minerals

MDPI

Article

Fluid Inclusion, Rare Earth Element Geochemistry, and Isotopic (O and S) Characteristics of the Ardakan Barite Deposit, Yazd Province, Iran

Ebrahim Ansari [1], Farhad Ehya [1,*], Ghodratollah Rostami Paydar [2] and Sara Maleki Kheymehsari [1]

[1] Department of Geology, Behbahan Branch, Islamic Azad University, Behbahan, Iran
[2] Department of Geology, Ahvaz Branch, Islamic Azad University, Ahvaz, Iran; rostamigsi2006@gmail.com
* Correspondence: ehya.farhad@iau.ac.ir

Abstract: The stratabound barite mineralization occurs in the Ardakan deposit as patches and veins in the dolomites and limestones of the Middle Triassic Shotori Formation. Rare-earth element (REE) geochemistry, O and S isotopes, and fluid inclusion data were used to identify the mode of barite formation. Barite is associated with subordinate fluorite and quartz and, to a lesser extent, with sphalerite, malachite, chrysocolla, and iron and manganese oxide-hydroxides. Barite contains a very low ∑REE concentration (14.80–19.59 ppm) and is enriched in light rare-earth elements (LREEs) relative to heavy rare-earth elements (HREEs). The low ∑REE content and the Ce/La ratio (4.0–6.5) indicate a hydrothermal (terrestrial) origin of the barite. Similar to barite, the ∑REE content in fluorite is low (0.14–6.52 ppm) and suggests a sedimentary setting. The Tb/Ca versus Tb/La diagram also indicates a hydrothermal origin of fluorite. The $\delta^{34}S$ values in the barite (+27.9 to +32.4‰) indicate that the sulfur most likely originates from evaporites and/or connate waters from the Late Precambrian to the Lower Cambrian. The $\delta^{18}O$ values (+15.9 to +18.1‰) in the barite show that the oxygen originated either from Late Precambrian–Lower Cambrian evaporites or from basinal brines with slightly higher $\delta^{18}O$ values than the evaporites. The salinity and homogenization temperature ranges of the aqueous fluid inclusions in barite, fluorite, and quartz (0.88–16.89 wt% NaCl equivalent and 90–270 °C, respectively) reveal that the mineralizing fluids were formed from basinal brines with the participation of heated meteoric water. From this, it is concluded that the Ardakan barite deposit was formed by the meeting of heated, ascending sulfate-bearing meteoric water and cooler, Ba-bearing connate water trapped in the overlying Middle Triassic dolomites and limestones. The Ardakan deposit belongs to the structure-related class and the unconformity-related subclass of barite deposits.

Keywords: rare-earth elements; fluid inclusions; sulfur isotopes; oxygen isotopes; barite; Ardakan

check for updates

Citation: Ansari, E.; Ehya, F.; Paydar, G.R.; Kheymehsari, S.M. Fluid Inclusion, Rare Earth Element Geochemistry, and Isotopic (O and S) Characteristics of the Ardakan Barite Deposit, Yazd Province, Iran. *Minerals* **2024**, *14*, 739. https://doi.org/10.3390/min14080739

Academic Editor: Norman Moles

Received: 22 June 2024
Revised: 20 July 2024
Accepted: 22 July 2024
Published: 24 July 2024

Copyright: © 2024 by the authors. Licensee MDPI, Basel, Switzerland. This article is an open access article distributed under the terms and conditions of the Creative Commons Attribution (CC BY) license (https://creativecommons.org/licenses/by/4.0/).

1. Introduction

Barite ($BaSO_4$) is the most important Ba-bearing mineral, followed by witherite ($BaCO_3$) as the second most common Ba mineral. Although witherite has a higher Ba content (77.7% BaO) than barite (65.7% BaO), Ba sulfate is economically more important than witherite, mainly because it is much more widespread than Ba carbonate [1,2]. With a theoretical density of 4.5 g/cm^3, barite is considered a heavy mineral. Barite is mainly used in the oil and gas drilling industry. Other applications of barite include additives in the medical industry, friction materials, paints, plastics, rubber and other products, shielding in X-ray and gamma-ray applications, and industrial chemicals. Barium is used in ceramic glazes, enamels, optical glass, primers, signal flares, steel hardeners, fluxes for welding, and a variety of other products [3–6].

With an average crustal abundance of 250 ppm, barium is a relatively abundant and widespread element in the Earth's crust [7,8]. Due to the similar ionic radius and electronegativity between Ba^{2+} and K^+ cations, these two cations show similar geochemical

signatures. Barium occurs in the Earth's crust mostly in solid solution for K in K-feldspars and K-micas, and substitutes Ca to a lesser extent in Ca-silicates. In the course of geological time from the Early Archean (~3.5 Ga) to the present, Ba-bearing aqueous fluids have obtained their Ba content from the leaching of silicate, carbonate, and sulfate minerals in sedimentary, metamorphic, and igneous rocks [8]. The mixing of these Ba-bearing fluids with a second oxidized, sulfate-bearing shallow fluid, such as seawater, has led to the formation of most of the barite present in the Earth's crust [8–10].

Barite occurs in a remarkably diverse range of sedimentary, metamorphic, and igneous geological environments, such that barite deposits have been categorized into several groups based on physical characteristics, geochemical properties, and geologic setting [2,3,8,11,12]. This complexity of origin requires a detailed dataset comprising geological, geochemical, fluid inclusion, and isotopic data to determine the conditions under which a barite deposit is formed. Data on fluid inclusions, the $\delta^{18}O$ and $\delta^{34}S$ isotopic composition, and the trace element geochemistry of barite help to identify the sources of the mineral-forming fluids and components as well as the environments of precipitation [8].

Iran has a large number of barite deposits and prospects, with a reserve of 24 Mt [13]. In recent years, some barite deposits have been studied in Iran [14–26]; however, there are still many large and small deposits that have not yet been studied in detail. Rahimpour Bonab and Shekarifard [27] and Shekarifard et al. [28] have studied barite and barite–chalcopyrite deposits in the Ardakan region, reporting that the host rock of these deposits is undifferentiated Upper Devonian–Lower Carboniferous and Permian limestones and dolomites. The Ardakan barite deposit is hosted by the Middle Triassic dolomites of the Shotori Formation, as shown in the official geological map of the region at 1:100,000 scale [29]. This contradiction means that we are not sure whether the above studies really refer to the deposit known as the Ardakan barite deposit, which we discuss in this study. However, Rahimpour Bonab and Shekarifard [27] assumed that the barite mineralization in the Ardakan area is related to the magmatic activities of the early Cimmerian orogeny. In this study, with a solid database consisting of geological and petrographic evidence, rare-earth element (REE) and O and S isotope geochemistry, and fluid inclusion results, we aim to decipher the genesis of the Ardakan barite deposit.

2. Geological Setting

2.1. Regional Geology

The Ardakan barite deposit, with the geographical coordinates 54°19′28″ east longitude and 32°24′23″ north latitude, is located 37 km northeast of the city of Ardakan, Yazd province, Iran. From a geological point of view, it is located in the Central Iran Zone (Figure 1). The Central Iran Zone is one of the most important tectono-sedimentary units in Iran. It is the most complex and geographically largest unit in Iran, comprising rocks from the Neoproterozoic to the Quaternary and showing several phases of orogeny, metamorphism, and magmatism [30]. The Central Iran Zone is a triangular region of the inner Iranian plateau and is bounded by the marginal fold-and-thrust belts of the Zagros and Makran in the south, the Alborz and Kopeh Dagh in the north, and the Sistan accretionary wedge in the east. The mountain ranges and depressions of central Iran are separated by deep-seated reverse and strike-slip faults [31]. From east to west, the Central Iran Zone consists of four major crustal domains, including the Lut Block, the Tabas Block, the Posht-e-Badam Block, and the Yazd Block, which are separated by a series of intersecting regional faults [32]. The Ardakan barite deposit is located in the central part of the Yazd Block (Figure 1).

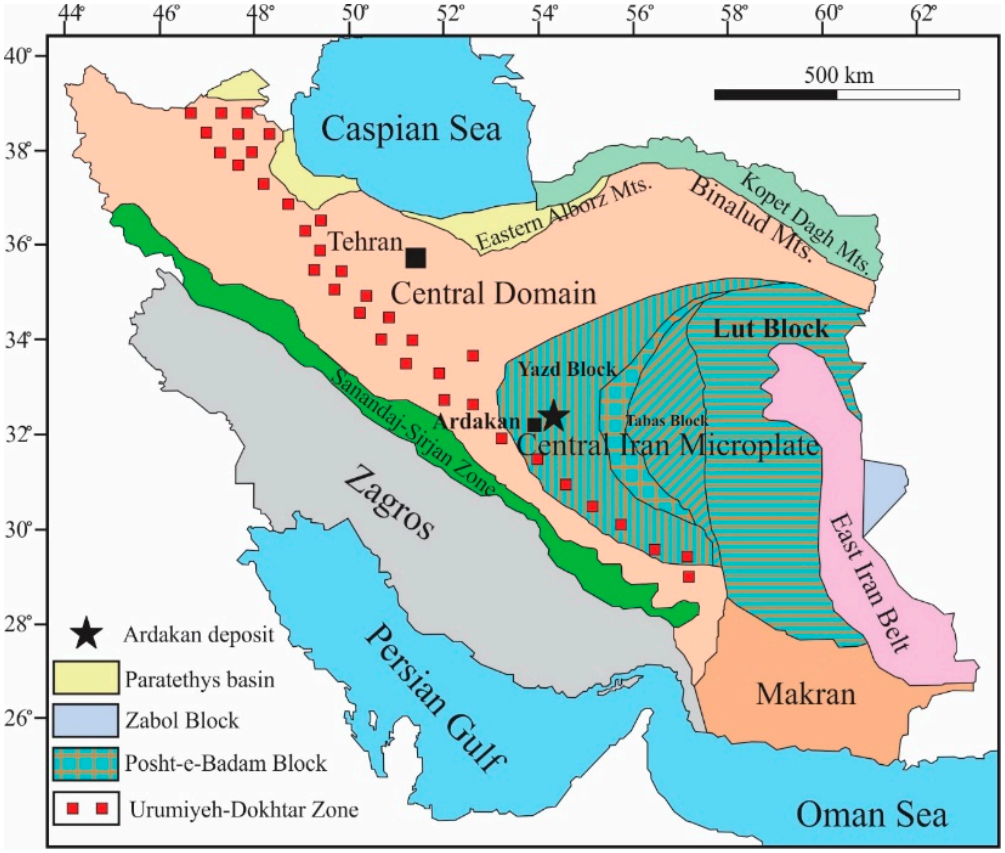

Figure 1. A map of the main tectonic zones of Iran with the location of the Ardakan barite deposit (modified after [33]).

2.2. Local Geology

The geological map of the area around the Ardakan barite deposit is shown in Figure 2 [29]. Various rock types from the Precambrian to the Quaternary occur in the area. The oldest rock unit from the Late Precambrian is a member of the Rizu Formation, which consists of metamorphosed siliciclastic and volcanoclastic rocks including rhyolite, tuff, and rhyolitic tuff. These rocks are overlain by three members of the Late Precambrian Dezu Formation that comprise, from bottom to top, (1) a sequence of carbonate rocks (usually metamorphosed dolomite), tuff, rhyolitic tuff, and other volcanoclastic rocks, and sometimes shale and sandstone beds; (2) thick layers of gypsum and thinly bedded dolomite; and (3) dolomitized, cherty stromatolitic limestone. The age of the third member of the Dezu Formation extends to the Lower Cambrian (Figure 2).

The Paleozoic in the studied area begins with strata from the Lower Cambrian, which consist of the following three members: (1) the lower member conformably overlays the Dezu Formation and begins with 3 m of alternating sandy shale, thinly bedded dolomite, chert veins, and thinly bedded quartzite, followed by 265 m of gypsiferous and clastic shales, slate, and phyllite with several layers of thinly bedded dolomite, rhyolitic lava, and rhyolitic tuff; (2) this member consists of gypsiferous shaley sandstones and interbeds of *metagraywacke* sandstones with a thickness of 85 m; and (3) the upper member consists mainly of coarse-grained, medium- to thick-bedded sandstones, some lithoclasts and volcanoclasts, and shale and metamorphosed micaceous sandstone on the top with a thickness of 400 m (Figure 2). The upper part of the Lower Cambrian to Middle Cambrian is represented by the Kuhbanan Formation, which is 80 to 120 m thick. Its lower contact lies conformably above the second member of the Lower Cambrian rock units, while it is unconformably covered by the Lower Devonian Padeha Formation. The Kuhbanan Formation in the region consists of five members, including the basal quartzite with a

thickness of 41 m; the lower dolomite, which consists of dolomite and cherty dolomite, and shale in the uppermost part with a thickness of 12–13 m; the middle shale, which contains an interval of shale and cherty dolomite, with a thickness of 22–23 m; the upper dolomite, which consists of massive dolomite with traces of stromatolites and benthic fossils in the upper part and a thickness of 21–22 m; and the upper shale, which consists of shale and a dolomite layer in the lower part with a thickness of about 40 m. The Devonian rock units include the Padeha and Bahram formations. The Lower Devonian Padeha Formation is 438 m thick and consists mainly of quartzite, sandstone, and intercalations of shale and dolomite. The lower contact of this formation lies unconformably on the Kuhbanan Formation and its upper contact is conformably covered by the Bahram Formation. The Upper Devonian Bahram Formation with a thickness of 110 m consists mainly of limestones, but also contains layers of *ferruginous* sandstone, tuff, lapilli tuff, basalt, and tuffaceous shale. The upper contact of this formation is characterized by a lateritic horizon with coarse pisolites, which represents an epeirogenic surface.

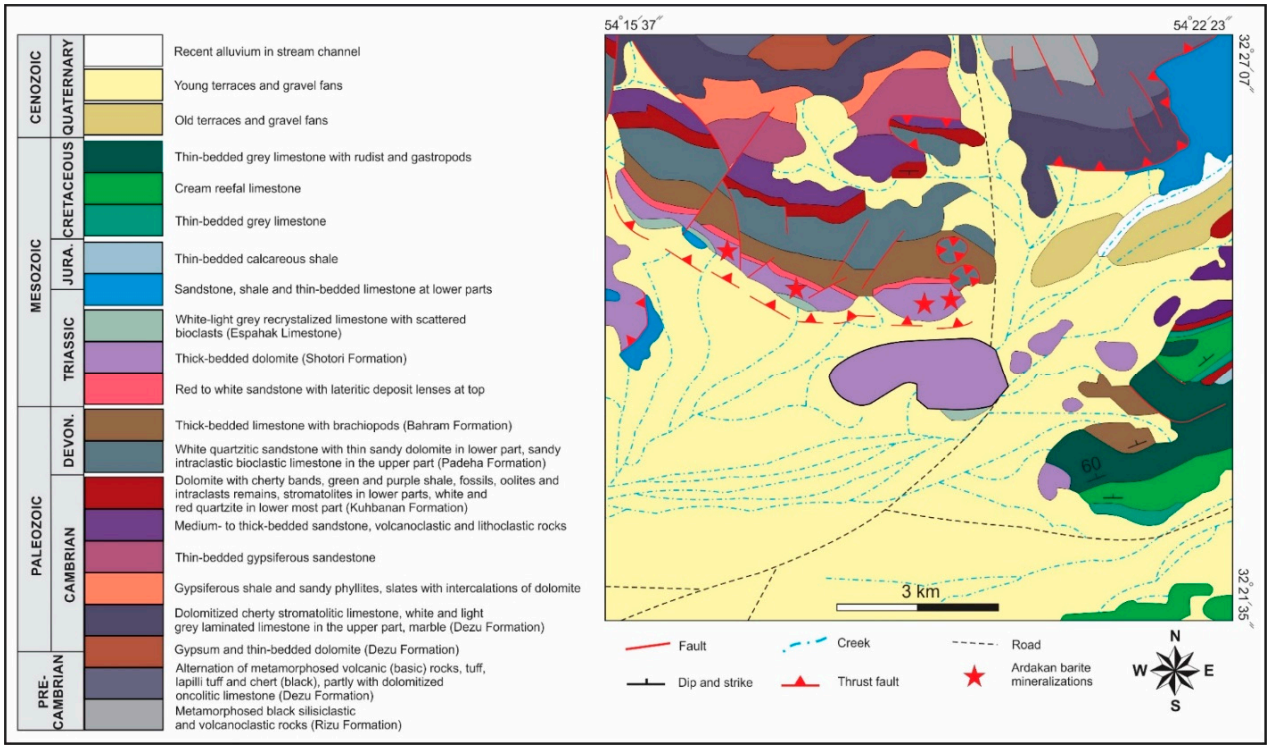

Figure 2. Simplified geologic map of the Ardakan area (modified after [29]).

The Mesozoic begins with a Lower Triassic rock unit consisting of siltstone and sandstone, which merges into laterite in the upper part. This unit is conformably below the Middle Triassic Shotori Formation. The Shotori Formation consists of limestone with horizons of tuff and lapilli tuff, dolomites, and dolomitic limestones. The Ardakan barite mineralization occurs in the carbonate rocks of the Shotori Formation (Figure 2). The Middle Triassic Espahak Limestone consists of thin- to medium-bedded, fine-grained dolomite and dolomitic limestone conformably overlying the Shotori Formation. The Espahak Limestone is unconformably overlain by a rock unit consisting of alternating shale, sandstone, and siltstone with limestone interbeds, dating from the Upper Triassic to the late Lower Jurassic. This unit is conformably covered by a 200–300 m thick rock unit consisting of calcareous shales with thin limestone layers from the Upper Jurassic. The Cretaceous rock units in the region comprise three units, the oldest of which consists of thin- to medium-bedded and sometimes slightly thick-bedded limestones as well as laminated calcareous shales from Aptian. It is overlain conformably by a Barremian–Aptian rock unit consisting of thick-bedded reefal limestones in the lower parts and massive ones in the upper parts. This

unit is overlain by the last Cretaceous rock unit in the area, which consists of thinly bedded limestones from the Barremian–Aptian (Figure 2).

The youngest deposits in the region are Quaternary deposits, consisting of old and young terraces and gravel fans, and alluvium in the streams.

Several orogenic phases have taken place in the area under investigation [29]. As already mentioned, the contact between the Kuhbanan and Padeha formations is an unconformity with an erosional surface. This unconformity is associated with the Caledonian orogenic phase. There is also a weak unconformity between the Bahram Formation and the Lower Triassic sandstone–laterite unit, resulting in a long time interval and an extensive stratigraphic gap between these two rock units. This stratigraphic gap can be attributed to the lack of sedimentation and continental erosion due to the Hercynian orogenic phase. A weak erosional discontinuity occurred between the Espahak Limestone and the Upper Triassic–Lower Jurassic shale and sandstone unit due to the effect of the early Cimmerian orogenic phase. There is an angular unconformity with a high angle to the vertical between the rock unit consisting of Triassic–Jurassic shales and sandstones and the Cretaceous rock units, which indicates the implementation of an intense orogenic phase in the late Cimmerian. The importance and intensity of this orogenic phase is reflected in the strong thrusts that occurred at this time. Finally, the stratigraphic gap between the Cretaceous and Cenozoic rock units is probably related to the Laramide orogenic phase.

Due to the occurrence of these orogenic phases, the area of the Ardakan barite deposit is a highly tectonized and faulted terrane. The most important structural feature in the study area is a series of thrusts and faults that are predominantly northwest–southeast trending, as well as some faults that are almost perpendicular to the formers. Most of these faults have a strike-slip function. The thrust faults have pushed older rock units, even from the Precambrian, onto younger units (Figure 2), which indicates the deep function of these faults.

2.3. Size and Geometry of the Orebody

According to the available data, the discovery of the Ardakan barite deposit apparently dates back to 1975. The proven reserve of this deposit is stated to be 705,000 tons, of which 365,000 tons have been mined and 340,000 tons remain. The barite mineralization occurred stratabound in the carbonate rocks of the Middle Triassic Shotori Formation in a 5 km long section, in which there are eight barite outcrops where quarries are established. Some of these quarries are currently inaccessible. Mining was carried out both in open pits and underground. The mineralization extends along a northwest–southeast trend, parallel to the major faults and thrusts (Figure 2). In the quarries, barite mineralization is observed as patches and veins ranging from several meters to several tens of meters in length and several tens of centimeters to several meters in thickness. Barite is mostly pure and has an average specific gravity of 4.2.

3. Materials and Methods

Field surveys were carried out to investigate the relationship between barite mineralization and the host rock, to select suitable samples for petrographic and mineralogical, geochemical, isotopic and fluid inclusion studies, as well as to examine the macroscopic properties of ore and host rock. A total of sixty minerals (barite, quartz, and fluorite), ore, and host rock samples were selected. To minimize the impact of the host rock on the geochemistry and temperature of mineral formation, mineral samples were taken as far away from the host rocks as possible. The samples were taken from different accessible quarries. Petrographic and mineralogical studies were carried out on 24 thin sections from ore and host rock samples using a Kyowa transmitted light polarizing microscope.

The concentrations of rare-earth elements (REEs), Y, and Sr were determined in eight barite and six carbonate host rock samples at the ZARAZMA Mahan laboratory (Kerman, Iran) using the ICP-MS method. For the host rock samples, the concentrations of major elements were also determined using the ICP-OES method. The clean barite samples

were taken from the crushed samples under a binocular microscope to keep the analyzed samples as pure as possible. The measurement uncertainty has a 95% confidence interval using the **internal reference materials**. The detection limits are 0.05 ppm for Gd, Pr, and Yb, 0.1 ppm for Sm, Dy, Er, Tm, Eu, Lu, and Tb, 0.5 ppm for Ce, Nd, and Y, and 1.0 for La and Sr. For all the major elements, the detection limit is 0.01%.

The concentration of REE and Y in seven fluorite samples was determined in the laboratory of Novin Shimyar Co., Ltd. (Tehran, Iran) using the ICP-MS method. Clean fluorite pieces were separated from the crushed samples under a binocular microscope. The separated samples were then pulverized as 85% of the sample passed through a 200 mesh sieve. A certain amount of the pulverized samples was dissolved using the four acids (HCl, HNO_3, $HCLO_4$, and HF) digestion method and measured. The uncertainty of the measurements using internal reference materials is within the 95% confidence interval with the confidence factor of k = 2. The detection limits are 0.05 ppm for Dy, Sm, and Pr, 0.1 ppm for Gd, Ho, Er, Tm, Yb, Lu, and Tb, 0.5 ppm for Eu, Ce, and Nd, and 5 ppm for Y and La. To determine the Ca concentration in fluorite samples, 0.1 g of the pulverized samples were dissolved with HCl in the vicinity of heat and measured using the titration method. The uncertainty of the measurements lies within the 95% confidence interval with a confidence factor of k = 2. The detection limit is 0.1%.

Six barite samples were analyzed for oxygen and sulfur isotopes using an isoprime isotope ratio mass spectrometer (Pyrocube, Elementar ®-Frankfurt, Germany) at the Stable Isotope Research Laboratory of Arak University, Iran. After the pure barite samples were pulverized, as 85% of the sample passed through a 200 mesh sieve, they were combusted in the elemental analyzer at 1150 °C to generate SO_2 and at 1450 °C to release oxygen from the samples in separate runs. All oxygen was converted to CO over carbon black and glassy carbon. The SO_2 and CO gasses are stripped of the water in the water trap. After all interfering gasses have been removed, they are finally fed into the isotope ratio mass spectrometer to be analyzed for sulfur and oxygen isotopes. Repeated measurements were performed on IAEA reference materials (IAEA-S-4 and IAEA-NBS-28) and a secondary laboratory standard to verify the whole procedure and to calibrate the reference gas. The certified $\delta^{34}S$ (‰) values for IAEA-S-4 and the secondary laboratory standard are $+16.9 \pm 0.2$ and -6.3 ± 0.2, respectively, compared to VCDT. The IAEA-NBS-28 standard has a certified $\delta^{18}O$ (‰) value of $+9.6 \pm 0.1$ compared to VSMOW. The standard deviations (1σ) for $\delta^{34}S$ and $\delta^{18}O$ are 0.2‰ and $\leq$0.3‰, respectively. The isotope ratios are reported in δ notation as per mil (‰) relative to VCDT for sulfur and VSMOW for oxygen.

Fluid inclusion studies were carried out on barite (Brt 1), fluorite (Flr 1), and quartz samples from the early mineralization stage. Three doubly polished wafers (~150 µm thick) were prepared from each mineral sample (nine wafers in total). A Zeiss microscope (Axioplan2, imaging) with a Linkam THMS-600 heating–freezing stage was used to examine fluid inclusions in the laboratory of the Iranian Mineral Processing Research Center (IMPRC) (Karaj, Iran). The instrument was calibrated using the standard material cesium nitrate with a melting point of +414 °C and n-hexane with a melting point of −94.3 °C, resulting in a precision of ±0.6 °C for heating and ±0.2 °C for freezing measurements. On the recommendation of Lawler and Crawford [34], the barite samples were first subjected to heating and then freezing studies, while the reverse was performed for fluorite and quartz samples. The ice-melting temperatures ($T_{m,ice}$) were used to calculate the salinities of the fluid inclusions according to the equation of Bodnar [35].

4. Results

4.1. Petrography and Mineralogy

4.1.1. Host Rocks

The barite mineralization occurs in the Ardakan deposit in the form of patches and veins in the carbonate rocks of the Middle Triassic Shotori Formation (Figure 3a,b). In the immediate vicinity of the barite orebodies, the Shotori Formation consists of dark gray, medium- to thick-bedded dolomites, and lesser limestones whose weathering color is light

brown to cream. Calcite veins in the host rocks have caused the formation of a zebra structure in places (Figure 3c). As can be seen in the open pits, the host rocks are highly faulted and fractured (Figure 3d). Fractures and faults are filled with iron oxides and hydroxides in places (Figure 3e). The contacts between the host rocks and the barite patches and veins are sharp. The host rocks have no evidence of hydrothermal alteration.

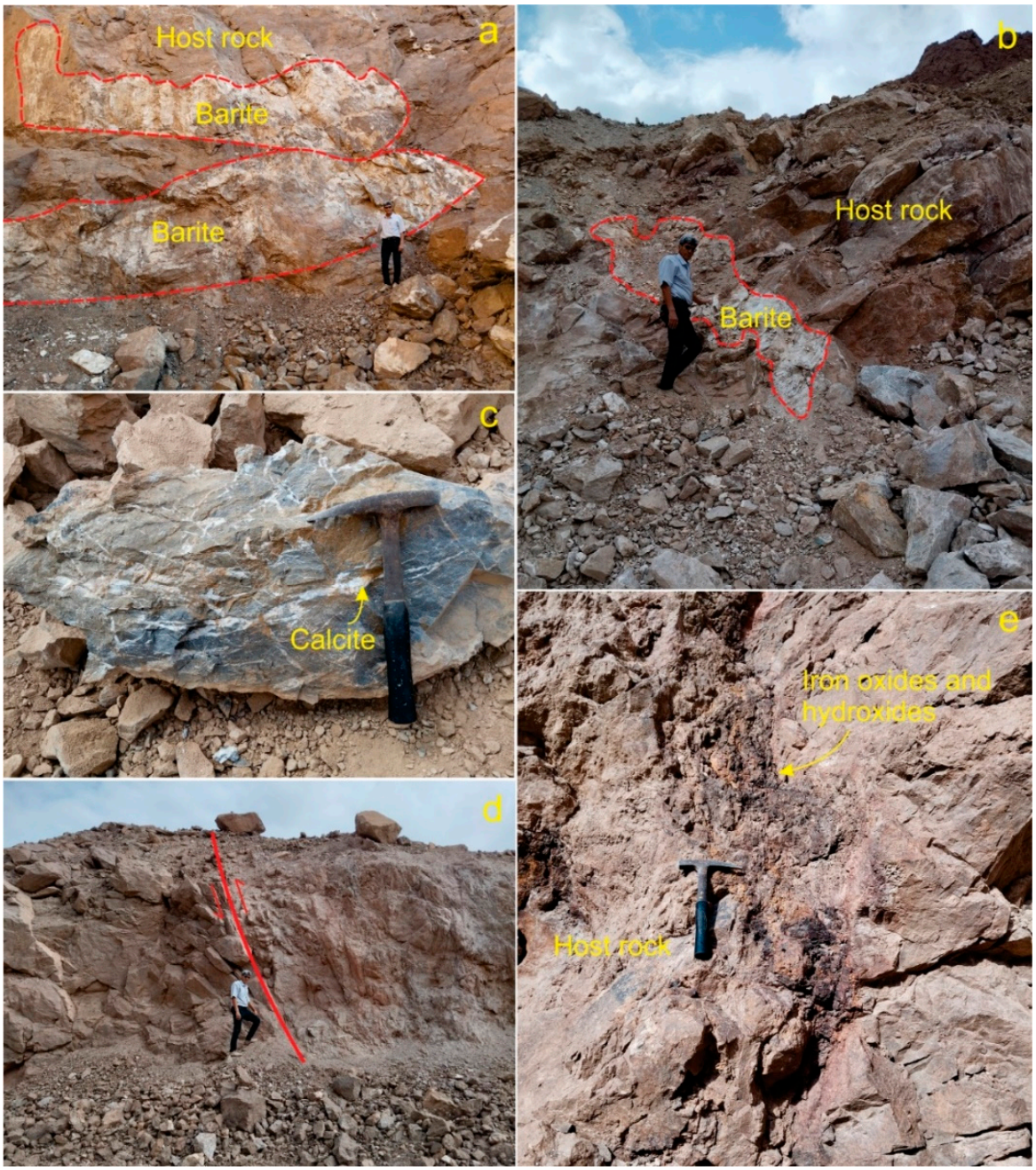

Figure 3. (**a**,**b**) Photographs showing barite veins and patches in the carbonate rocks of the Shotori Formation. (**c**) Photograph showing calcite veins in the carbonate host rocks with a zebra structure. (**d**) Photograph showing a thrust fault in the carbonate host rocks. (**e**) Photograph showing fractures in the carbonate host rocks filled with iron oxides and hydroxides.

Microscopic examinations show that the carbonate host rocks are petrographically diverse and comprise different rock types. They generally consist of dolosparite with large dolomite crystals, sometimes impregnated with iron oxides and hydroxides. Near the orebody, the spaces between the dolomite crystals are filled with barite crystals (Figure 4a).

Dolomitized limestone is another type of host rock; it consists of a matrix that contains medium-grained calcite and dolomite crystals and in which coarse calcite, dolomite, and quartz crystals also occur locally (Figure 4b). In places, the host rock consists of a micritic matrix (mudstone) containing coarse veinlets of sparry calcite and quartz crystals (Figure 4c). Small tubular barite and anhedral quartz crystals are sometimes found in the mudstones (Figure 4d). In other places, the host rock consists of calcarenite, which contains iron oxides and hydroxides both in the form of patches and veinlets (Figure 4e). Due to local recrystallization, the carbonate matrix of calcarenites has sometimes formed coarse calcite crystals up to 4 mm in size. According to the petrographic investigations, the wall-rock alteration includes recrystallization, silicification, and baritization. Obviously, these alterations are associated with the hydrothermal phase that led to barite mineralization in the studied area.

4.1.2. The Ore

The ore in the Ardakan deposit consists essentially of barite with the accompanying minerals fluorite, quartz, sphalerite, malachite, chrysocolla, and iron and manganese oxide-hydroxides. Nevertheless, the proportion and distribution of accessory minerals is not uniform in all quarries, so that either all or some of them do not occur in some places. In addition to the above minerals, Rahimpour Bonab and Shekarifard [27] and Shekarifard et al. [28] reported many other accessory minerals in the barite deposits from the Ardakan area, including chalcopyrite, chalcocite, pyrite, covellite, yarrowite, spionkopite, geerite, anilite, azurite, cuprite, goethite, lepidocrocite, gold, dolomite, and calcite. However, if the deposits studied by these researchers include the deposit investigated here, none of the minerals mentioned are observed in the current mining levels.

Barite commonly makes up >90% of the volume of the ore. It usually occurs in pure massive and crystalline patches with white, colorless, and pink color (Figure 5a). The crystalline masses of barite often show perfect rhombic cleavage (Figure 5b). The veiny nature of the barite mineralization can also be seen at the centimeter scale (Figure 5c). At the contact of the barite orebodies with the wallrock, the crushed host rock is cemented by barite as breccia, showing that the barite mineralization is epigenetic (Figure 5d). Fluorite occurs locally as crystalline patches of colorless, pale to deep purple, and pale green color. Although it was mined in tens of tons in the upper levels of the deposit, it can only be seen as an accessory mineral (<10% of the ore) in some places in the current mining levels. Apparently, the fluorite content decreases with increasing depth. Fluorite usually coexists with barite (Figure 5e), but can also be seen in places in the form of crystals growing as small geodes in the cavities of the rock (Figure 5f). This indicates that fluorite formed in two generations, one at the same time as barite (Flr 1 in Figure 6) and the other in a late phase in open spaces (Flr 2 in Figure 6), probably due to remobilization. Quartz also occurs locally as colorless to milky massive and crystalline masses (Figure 5g). However, quartz occurs in places in larger quantities as sugar-grained aggregates, which cause intense silicification of the host rock. Sphalerite is a rare mineral that occurs locally as massive patches (Figure 5e). In general, barite, fluorite, quartz, and sphalerite are intergrown, showing that they formed almost simultaneously during mineralization.

Malachite and chrysocolla usually occur as druses and coatings on any available surface of the preexisting minerals (Figure 5f,h–j). Iron oxide-hydroxides are commonly found as rusts and coatings (Figure 5g,h). Manganese oxides occur in the form of coatings and dendritic aggregates on the surfaces of preexisting minerals (Figure 5j). The fact that malachite, chrysocolla, and Fe- and Mn-oxides occur on the surface of preexisting minerals indicates that they were formed at a later stage of mineralization.

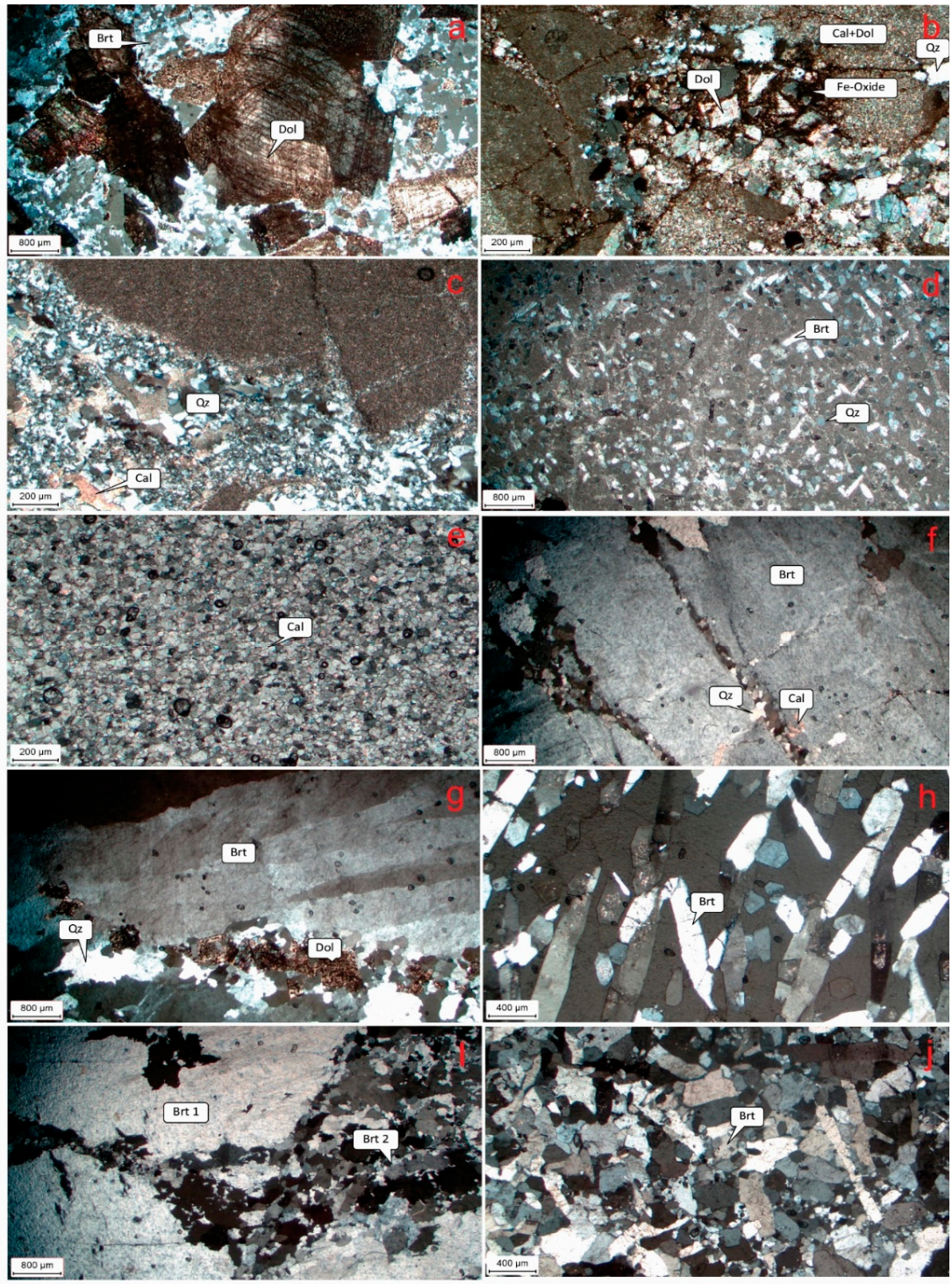

Figure 4. (**a**) Photomicrograph showing a dolosparite host rock with the spaces between dolomite crystals filled by barite. (**b**) Photomicrograph showing a dolomitized limestone with local coarse dolomite and quartz crystals. (**c**) Photomicrograph showing a mudstone containing coarse veinlets of sparry calcite and quartz crystals. (**d**) Photomicrograph showing a mudstone with small tubular barite and quartz crystals. (**e**) Photomicrograph showing a calcarenite containing small patches of iron oxides and hydroxides. (**f**,**g**) Photomicrographs showing large tubular barite crystals with quartz, calcite, and dolomite filling the spaces between barite crystals. (**h**) Photomicrograph showing small tubular barite crystals. (**i**) Photomicrograph showing the first (Brt 1) and the second generations (Brt 2) of barite crystals; and (**j**) equal-dimension barite crystals forming a granular texture. All photomicrographs in XPL. Brt = barite, Dol = dolomite, Cal = calcite, and Qz = quartz.

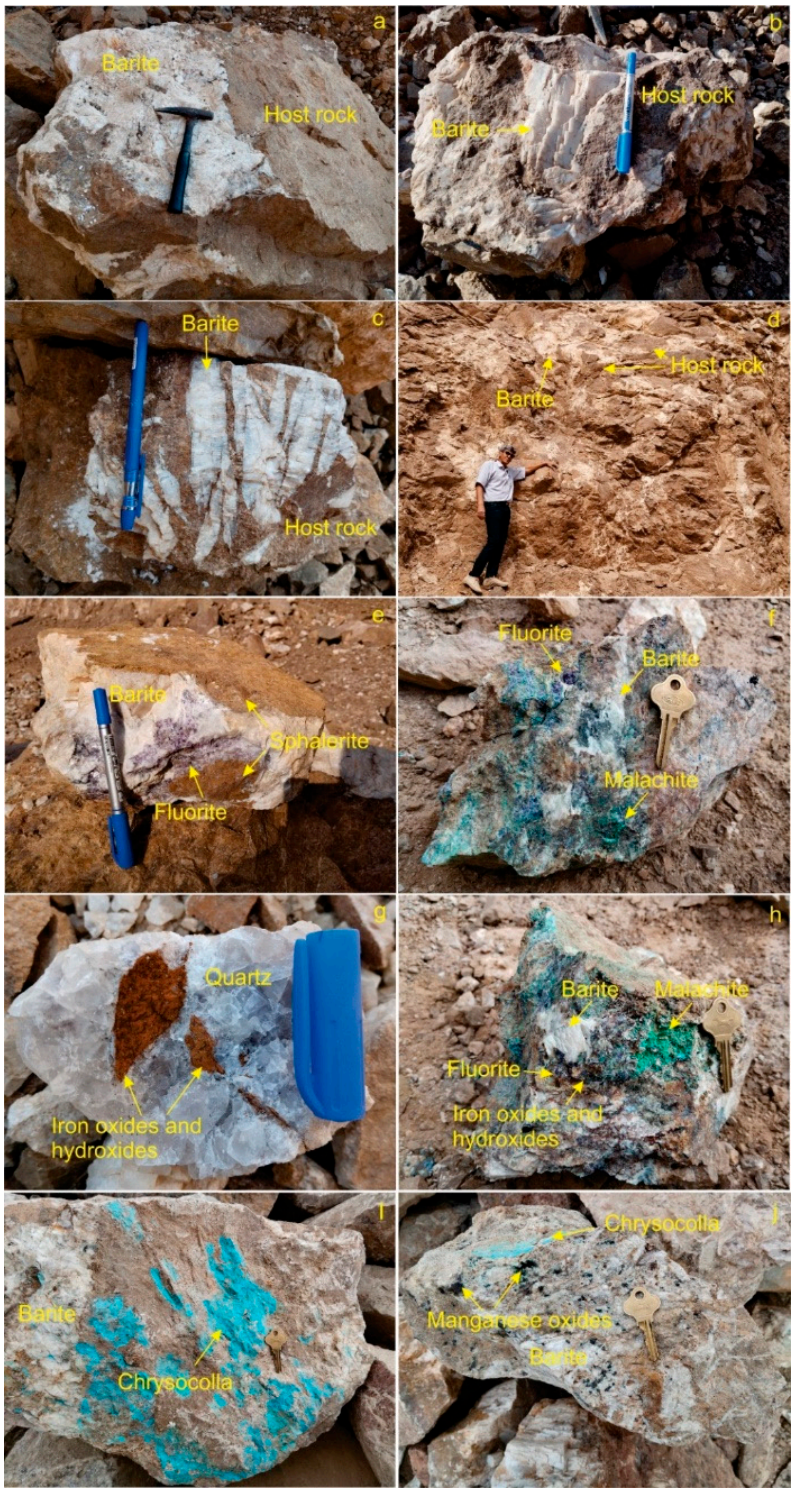

Figure 5. (**a**) Photograph showing a pure crystalline patch of barite. (**b**) Photograph showing a crystalline patch of barite with perfect rhombic cleavage. (**c**) Photograph showing a veiny barite mineralization at the centimeter scale. (**d**) Photograph showing brecciated carbonate host rocks cemented by barite. (**e**) Photograph showing barite with fluorite and sphalerite. (**f**) Photograph showing barite with fluorite and malachite. (**g**) Photograph showing quartz and iron oxides and hydroxides. (**h**) Photograph showing barite with iron oxides and hydroxides, malachite, and fluorite. (**i**) Photograph showing barite with chrysocolla. (**j**) Photograph showing barite with manganese oxides and chrysocolla.

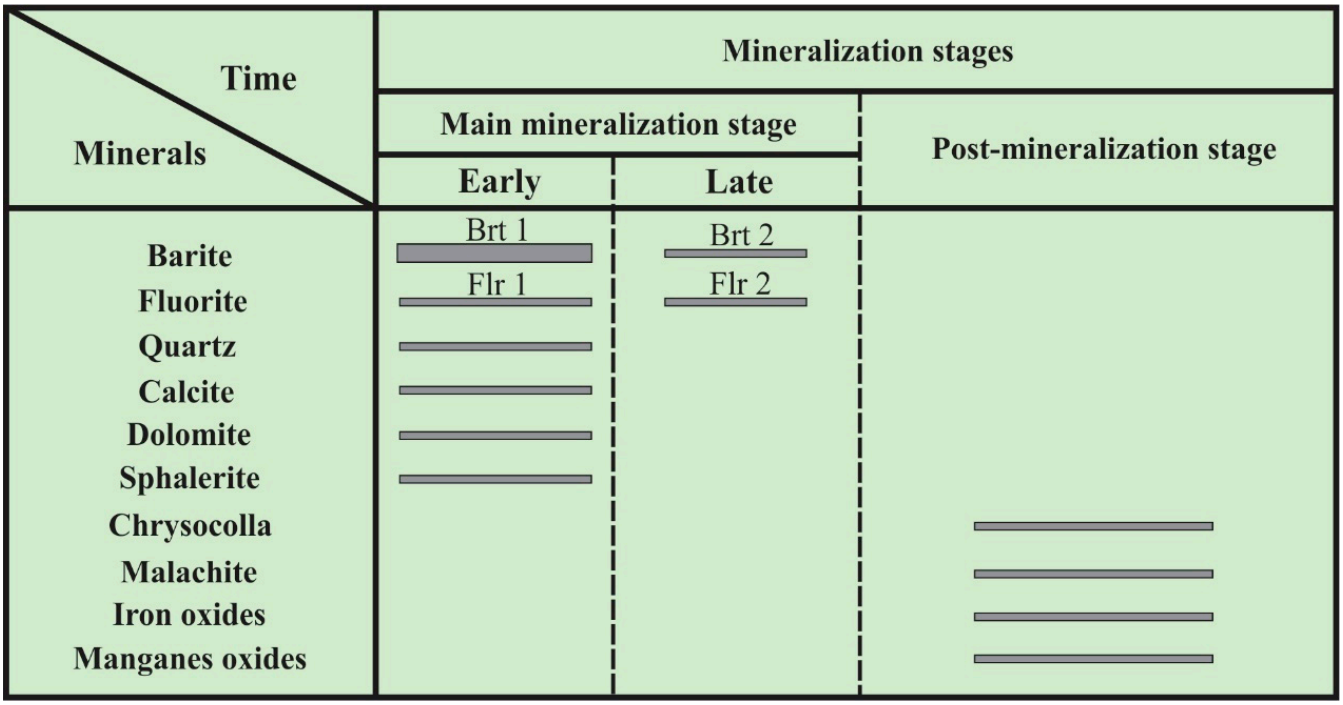

Figure 6. Paragenetic sequence of the ore from the Ardakan deposit.

Microscopic studies show that barite consists of crystals of various sizes and shapes. In some samples, barite shows large tubular crystals (several millimeters in length), which usually make up more than 90% of the sample by volume. In the spaces between barite crystals, quartz, calcite, and dolomite are formed in the form of fine (<600 μm) anhedral to euhedral crystals (Figure 4f,g). Tubular crystals are not necessarily always large, but in places they form small (100 to >1000 μm) euhedral to subhedral crystals (Figure 4h). In some samples, barite appears to be composed of two generations; the first generation (Brt 1 in Figure 6) is the coarse barite crystals, whose dimensions reach >3 mm, and the second generation (Brt 2 in Figure 6) is the fine barite crystals, which is formed in the spaces between the coarse barite crystals (Figure 4i). In places, barite is composed of anhedral to euhedral crystals of relatively equal dimensions (50 to 800 μm), which form a granular texture (Figure 4j). Barite crystals are usually pure, rarely with very small inclusions of carbonate materials. This suggests that barite was emplaced preferentially as open-space-filling rather than as replacement of the host rocks.

The paragenetic sequence of the ore is shown in Figure 6. Based on textural evidence, two mineralization stages can be distinguished, namely, the main mineralization stage and the post-mineralization stage. The main mineralization stage consists of two sub-stages, an early and a late stage, with barite (Brt 1), fluorite (Flr 1), quartz, calcite, dolomite, and sphalerite being formed in the early sub-stage, and minor barite (Brt 2) and fluorite (Flr 2) in the late sub-stage. The deposition of malachite, chrysocolla, iron and manganese oxides, and hydroxides took place in the post-mineralization (supergene) stage.

4.2. Mineral Chemistry

4.2.1. Barite

The concentrations of REEs, Y, and Sr in the barite samples are presented in Table 1. With the exception of La, Ce, Sm, Eu, and Gd, the concentration of the other REEs and of Y in the samples is below the detection limit. For the REEs detected, the ∑REE values are low and range from 14.80 to 19.59 ppm with a mean value of 16.90 ppm. Censored data in Table 1 show that the maximum ∑REE concentration for all REEs in the barite samples can only be about 1 ppm higher than this range. Since the detected REEs are LREEs, and the HREE concentration in the samples is below the detection limit, it is concluded that barite

samples are enriched in LREEs compared to HREEs. The Ce/La ratio varies between 4.0 and 6.5 in the barite samples. The Sr concentrations range from 1008 to 2709 ppm with a mean value of 1672 ppm, indicating that barites belong to the barite end member in the barite–celestite solid solution series.

Table 1. The concentrations of REEs, Y, and Sr (ppm) in the barite samples from the Ardakan deposit (n.d. = not determined).

Sample	B-3-8	B-3-10	B-4-5	B-4-6	B-5-3	B-5-4	B-6-2	B-6-4
La	2	2	2	2	2	2	2	2
Ce	8	8	10	10	9	8	11	13
Pr	<0.05	<0.05	<0.05	<0.05	<0.05	<0.05	<0.05	<0.05
Nd	<0.5	<0.5	<0.5	<0.5	<0.5	<0.5	<0.5	<0.5
Sm	1.9	2.6	2.4	2.0	2.7	3.0	2.5	0.6
Eu	1.77	2.12	1.97	1.81	2.35	2.57	2.80	0.95
Gd	1.27	1.26	1.27	1.26	1.23	1.23	1.29	1.35
Tb	<0.1	<0.1	<0.1	<0.1	<0.1	<0.1	<0.1	<0.1
Dy	<0.1	<0.1	<0.1	<0.1	<0.1	<0.1	<0.1	<0.1
Ho	n.d.	n.d.	n.d.	n.d.	n.d.	n.d.	n.d.	n.d.
Er	<0.1	<0.1	<0.1	<0.1	<0.1	<0.1	<0.1	<0.1
Tm	<0.1	<0.1	<0.1	<0.1	<0.1	<0.1	<0.1	<0.1
Yb	<0.05	<0.05	<0.05	<0.05	<0.05	<0.05	<0.05	<0.05
Lu	<0.1	<0.1	<0.1	<0.1	<0.1	<0.1	<0.1	<0.1
Y	<0.5	<0.5	<0.5	<0.5	<0.5	<0.5	<0.5	<0.5
Sr	1691	1429	1709	2020	1594	1008	1216	2709
∑REE	14.94	15.98	17.64	17.07	17.28	14.80	19.59	17.90
Ce/La	4	4	5	5	4.5	4	5.5	6.5

4.2.2. Fluorite

The concentrations of REEs, Y, and Ca in the fluorite samples are listed in Table 2. The REE and Y concentrations in most of the fluorite samples are below the detection limit. The ∑REE values for the detected REEs are low and range from 0.14 to 6.52 ppm with a mean value of 1.26 ppm. Censored data in Table 2 indicate that the maximum ∑REE values for all REEs in the fluorite samples are less than 7 ppm higher than this range. The Y concentrations in two samples are 5 and 9 ppm. Calcium concentrations in the fluorite samples range from 48.00 to 51.10%. Since the Tb and La concentrations in the fluorite samples are below the detection limits, $\frac{3}{4}$ of the lower detection limit values are replaced with censored Tb and La data to calculate the Tb/Ca and Tb/La ratios. The Tb/Ca ratio ranges from 1.46×10^{-7} to 1.56×10^{-7}, while the Tb/La ratio in the fluorite samples is 0.02.

4.2.3. Host Rocks

The concentrations of major elements, REEs, Y, and Sr in the host rock samples are shown in Table 3. The SiO_2 concentration in the samples varies between 0.19 and 3.00%, except for one sample where the concentration is 35.04%, showing that it is highly silicified. The Al_2O_3 concentration is between 0.05 and 2.40%, indicating a low content of clay minerals in the samples. The BaO content is low and ranges from 0.01 to 0.61%. With the exception of one sample, in which the CaO content is high (55.03%) and the MgO content is low (0.21%), the CaO and MgO values are almost close to the stoichiometric composition of dolomite (30.41% CaO and 21.86% MgO) in the other samples. The host rocks, therefore, consist predominantly of dolomite with small amounts of limestone, which is consistent

with the lithology of the Shotori Formation. The values of Fe_2O_3 and LOI are in the ranges of <0.01 to 2.49% and 29.23 to 47.29%, respectively. The concentrations of K_2O, Na_2O, MnO, and TiO_2 are below 0.5%, with the exception of one sample in which the K_2O content reaches up to 0.63%.

Table 2. The concentrations of Ca (%), REEs, and Y (ppm) in the fluorite samples from the Ardakan barite deposit.

Sample	F-3-1	F-3-2	F-3-3	F-3-4	F-3-5	F-3-6	F-4-1
La	<5	<5	<5	<5	<5	<5	<5
Ce	6.34	<0.5	<0.5	<0.5	<0.5	<0.5	<0.5
Pr	<0.05	<0.05	<0.05	<0.05	<0.05	<0.05	0.05
Nd	<0.5	<0.5	<0.5	<0.5	<0.5	0.57	<0.5
Sm	<0.05	<0.05	<0.05	<0.05	<0.05	<0.05	0.08
Eu	<0.5	<0.5	<0.5	<0.5	<0.5	<0.5	<0.5
Gd	0.11	<0.1	<0.1	0.14	<0.1	<0.1	0.19
Tb	<0.1	<0.1	<0.1	<0.1	<0.1	<0.1	<0.1
Dy	0.07	<0.05	<0.05	0.16	0.07	0.06	0.13
Ho	<0.1	<0.1	<0.1	<0.1	<0.1	<0.1	<0.1
Er	<0.1	0.14	0.14	<0.1	0.18	0.4	<0.1
Tm	<0.1	<0.1	<0.1	<0.1	<0.1	<0.1	<0.1
Yb	<0.1	<0.1	<0.1	<0.1	<0.1	<0.1	<0.1
Lu	<0.1	<0.1	<0.1	<0.1	<0.1	<0.1	<0.1
Y	<5	<5	<5	9	<5	<5	5
Ca	48.00	51.10	50.00	49.60	48.40	50.00	49.20
∑REE	6.52	0.14	0.14	0.30	0.25	1.03	0.45
Tb/Ca	1.56×10^{-7}	1.46×10^{-7}	1.50×10^{-7}	1.51×10^{-7}	1.55×10^{-7}	1.50×10^{-7}	1.52×10^{-7}
Tb/La	0.02	0.02	0.02	0.02	0.02	0.02	0.02

The concentration of Nd, Tb, and Lu is below the detection limit in all host rock samples (Table 3). The ∑REE values are low and range from 13.39 to 24.60 ppm with a mean value of 18.80 ppm for the detected REEs. The ΣLREE and ΣHREE concentrations range from 13.29 to 24.4 and from 0.1 to 0.87 ppm, respectively. The LREE/HREE ratio in the host rock samples varies from 23.96 to 132.9, suggesting that they are enriched in LREE compared to HREE. Yttrium (Y) concentration ranges from <0.5 to 2 ppm, with a mean value of 1.12 ppm. The Sr concentration varies from 83 to 407 ppm with a mean value of 205.8 ppm. The Ce/La ratio varies between 2.0 and 2.4 in the host rock samples (Table 3). The chondrite-normalized [36] REE patterns for host rock samples are shown in Figure 7.

Table 3. The concentrations of major elements (%), REEs, Y, and Sr (ppm) in the host rock samples from the Ardakan barite deposit (n.d. = not determined).

Sample	HS-3-2	HS-4-2	HS-4-3	HS-5-1	HS-6-1	HS-6-2
			Trace elements			
La	5	5	6	5	5	4
Ce	11	10	13	11	12	8
Pr	0.47	0.32	0.25	0.49	0.33	<0.05

Table 3. *Cont.*

Sample	HS-3-2	HS-4-2	HS-4-3	HS-5-1	HS-6-1	HS-6-2
Nd	<0.5	<0.5	<0.5	<0.5	<0.5	<0.5
Sm	<0.1	<0.1	<0.1	<0.1	3	<0.1
Eu	<0.1	<0.1	<0.1	<0.1	2.67	<0.1
Gd	1.38	1.45	1.6	1.34	1.4	1.29
Tb	<0.1	<0.1	<0.1	<0.1	<0.1	<0.1
Dy	<0.1	0.1	0.2	<0.1	<0.1	<0.1
Ho	n.d.	n.d.	n.d.	n.d.	n.d.	n.d.
Er	0.2	0.1	0.3	0.1	0.2	0.1
Tm	<0.1	<0.1	0.1	<0.1	<0.1	<0.1
Yb	0.12	0.15	0.27	<0.05	<0.05	<0.05
Lu	<0.1	<0.1	<0.1	<0.1	<0.1	<0.1
Y	0.5	0.6	2	<0.5	1.4	<0.5
Sr	83	140	162	407	219	224
∑REE	18.17	17.02	21.72	17.93	24.6	13.39
∑LREE	17.85	16.77	20.85	17.83	24.4	13.29
∑HREE	0.32	0.25	0.87	0.1	0.2	0.1
LREE/HREE	55.78	67.08	23.96	178.3	122	132.9
Ce/La	2.2	2	2.16	2.2	2.4	2
Major elements						
SiO_2	3.00	2.53	35.04	0.57	0.42	0.19
Al_2O_3	0.61	0.22	2.40	0.05	0.14	0.05
BaO	0.01	0.01	0.03	0.08	0.61	0.08
CaO	28.60	28.74	18.27	55.03	30.30	30.43
Fe_2O_3	1.39	2.49	2.33	<0.01	1.30	0.57
K_2O	0.09	0.04	0.63	<0.01	0.03	<0.01
MgO	20.36	19.96	11.57	0.21	21.09	21.13
MnO	0.10	0.24	0.13	0.02	0.07	0.05
Na_2O	0.22	0.06	0.13	0.12	0.34	0.12
TiO_2	0.02	<0.01	0.12	<0.01	0.01	<0.01
LOI	45.60	45.70	29.23	43.79	45.03	47.29
Sum	100	99.99	99.88	99.87	99.34	99.91

4.3. Oxygen and Sulfur Isotope Systematics

The $\delta^{18}O$ and $\delta^{34}S$ isotope values of the barite samples are provided in Table 4. The $\delta^{18}O$ and $\delta^{34}S$ values are within the narrow ranges of +15.9 to +18.1‰ and +27.9 to +32.4‰, respectively.

Table 4. Oxygen and sulfur isotopic compositions of barite samples from the Ardakan deposit.

Sample	$\delta^{18}O_{VSMOW}$ (‰) ± 1σ	$\delta^{34}S_{VCDT}$ (%) ± 1σ
B-4-2	+15.9 ± 0.2	+29.0 ± 0.2
B-3-3	+17.8 ± 0.2	+32.4 ± 0.2
B-6-1	+16.1 ± 0.1	+29.9 ± 0.2

Table 4. *Cont.*

Sample	$\delta^{18}O_{VSMOW}$ (‰) ± 1σ	$\delta^{34}S_{VCDT}$ (%) ± 1σ
B-3-1	+16.0 ± 0.2	+27.9 ± 0.2
B-5-2	+17.6 ± 0.2	+28.8 ± 0.1
B-6-3	+18.1 ± 0.1	+29.9 ± 0.2

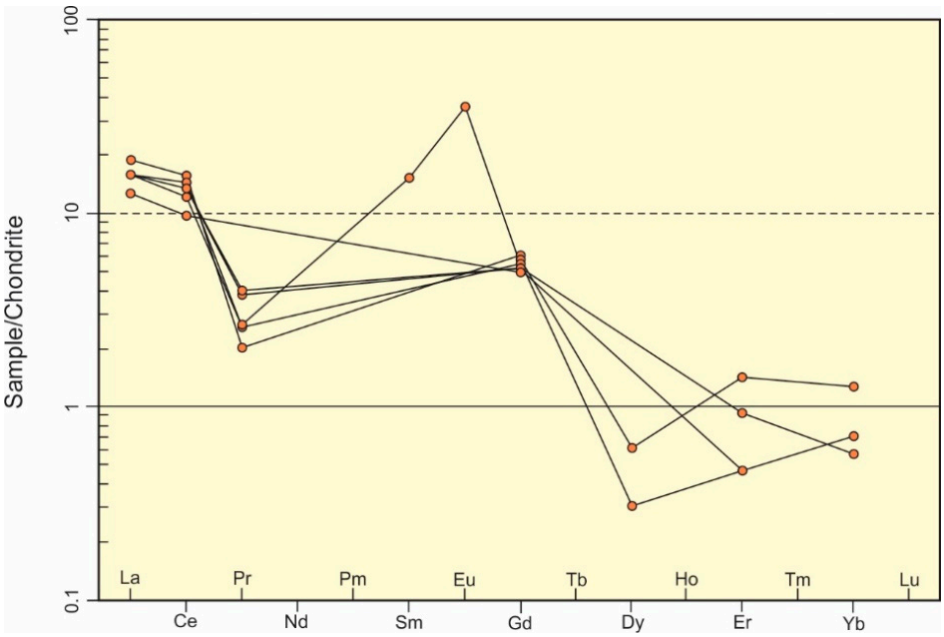

Figure 7. Chondrite-normalized [36] REE patterns for carbonate host rocks from the Ardakan deposit.

4.4. Fluid Inclusion Studies

4.4.1. Petrography of Fluid Inclusions

Using the criteria given by Roedder [37] and Shepherd et al. [38], two types of primary and secondary fluid inclusions were identified in barite, fluorite, and quartz samples from the Ardakan deposit. The distribution of the primary fluid inclusions is random or occurs individually, while the secondary fluid inclusions are often arranged along a line (Figure 8a). Since the secondary fluid inclusions show the post-formation history of the minerals, all microthermometric measurements were carried out on the primary fluid inclusions. The measured fluid inclusions occur as fluid inclusion assemblages (FIAs) with similar liquid–vapor ratios [39], commonly in single or rarely in multiple adjacent crystals. Based on the type and number of phases present in the fluid inclusions at room temperature and the behavior of the inclusions during the heating and cooling studies, only aqueous, liquid-rich biphase inclusions (L+V) were found in barite, fluorite, and quartz samples. These fluid inclusions have a dominant liquid phase (L) and a vapor bubble (V). The vapor phase accounts for 10 to 30 vol.% of the fluid inclusions. The size of the inclusions is between 5 and 30 μm, and they are found in irregular, elongated, and negative crystal shapes (Figure 8b–d).

4.4.2. Microthermometric Results

Microthermometric measurements were performed on liquid-rich biphase fluid inclusions (L+V) in barite, fluorite, and quartz samples. A total of 125 fluid inclusions (59 in barite, 35 in fluorite, and 31 in quartz) were measured. Table 5 contains the results of the microthermometry of fluid inclusions and abbreviations of the terms used in the text. To ensure complete freezing of the fluid inclusions during the cooling studies, they were

cooled to −110 to −100 °C. During the heating studies, all fluid inclusions were totally homogenized into the liquid phase.

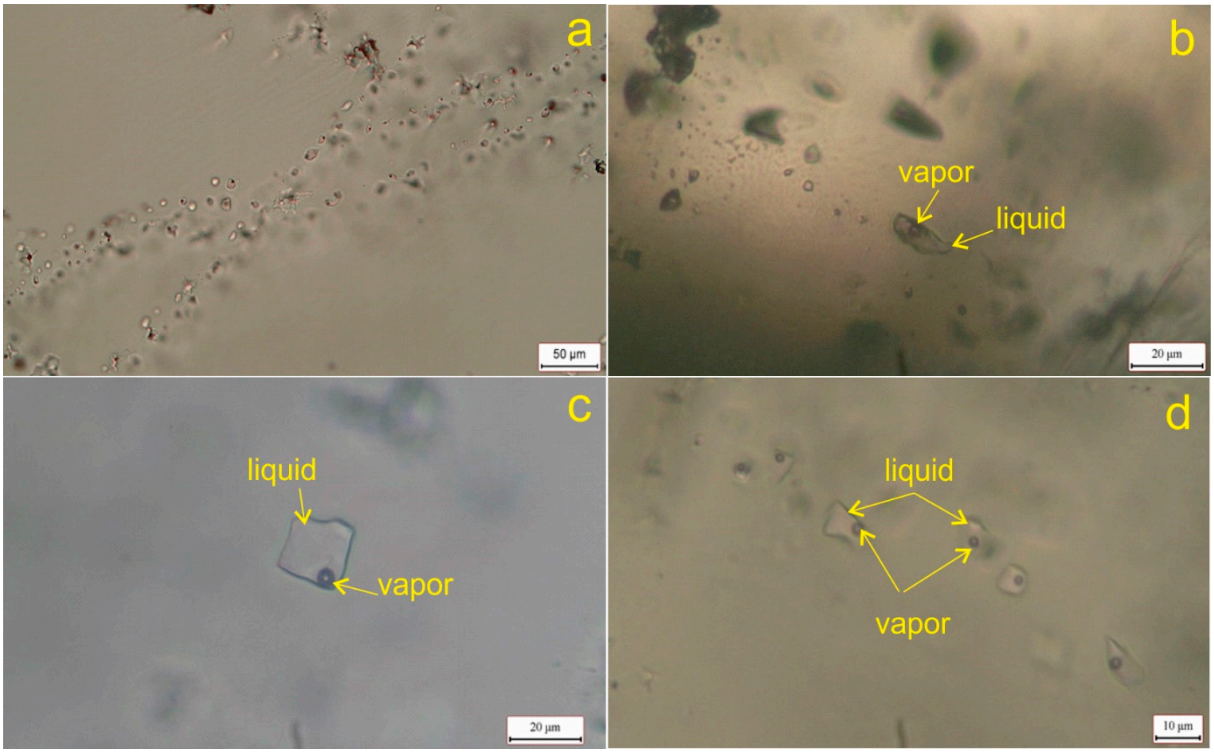

Figure 8. (**a**) Secondary fluid inclusions with a linear trend in fluorite. (**b**) Liquid-rich biphase fluid inclusion (L+V) with irregular shape in barite. (**c**) Liquid-rich biphase fluid inclusion (L+V) with negative crystal shape in fluorite. (**d**) Irregularly shaped biphase liquid-rich fluid inclusions (L+V) in quartz.

Table 5. Summary of the microthermometric results of fluid inclusions from the Ardakan barite deposit.

Host Mineral	T_e (°C)	$T_{m,ice}$ (°C)	T_h (°C)	Salinity (wt. % NaCl eq.)	N
Barite	−30/−21	−6.0/−0.5	138/270	0.88/9.21	59
Fluorite	−45/−30	−9.2/−2.5	92/220	4.18/13.07	35
Quartz	−40/−30	−13.5/−9.0	90/165	12.85/16.89	31

T_e: first ice-melting; $T_{m,ice}$: last ice-melting; T_h: homogenization to liquid; N: number of measurements.

The first ice-melting temperature (T_e) in barite-hosted fluid inclusions is in the range of −30 to −21 °C, indicating the presence of a H_2O–NaCl brine system with possible divalent cations such as Ca^{2+} and Mg^{2+} in the fluid inclusions [38]. The values of the last ice-melting temperature ($T_{m,ice}$) vary between −6.0 and −0.5 °C. The calculated salinity of the fluid inclusions based on the values of $T_{m,ice}$ is between 0.88 and 9.21 wt.% NaCl equivalent, with the highest frequency at 3 wt.% NaCl equivalent (Figure 9a). The homogenization temperatures (T_h) of fluid inclusions range from 138 to 270 °C, with the highest frequency at 175 °C (Figure 9b). The T_e values in fluorite-hosted fluid inclusions are in the range of −45 to −30 °C, showing the existence of a H_2O–NaCl brine system with possible cations Ca^{2+}, Mg^{2+}, Fe^{2+}, and K^+ in fluid inclusions [38]. The $T_{m,ice}$ values are in the range of −9.2 to −2.5 °C. The salinity of the fluid inclusions varies between 4.18 and 13.07 wt.% NaCl equivalent, with the highest frequency at 7 wt.% NaCl equivalent (Figure 9a). The T_h of the fluid inclusions ranges from 92 to 220 °C, with the highest frequency at 135 °C (Figure 9b). In quartz-host fluid inclusions, T_e values range from −40 to −30 °C and

indicate the presence of a H_2O–NaCl brine system with possible cations Ca^{2+}, Mg^{2+}, Fe^{2+}, and K^+ in fluid inclusions [38]. The $T_{m,ice}$ values are in the range of −13.5 °C to −9.0 °C. The salinity of the fluid inclusions varies between 12.85 and 16.89 wt.% NaCl equivalent, with the highest frequency at 16 wt.% NaCl equivalent (Figure 9a). The T_h values range from 90 to 165 °C, with the highest frequency at 115 °C (Figure 9b).

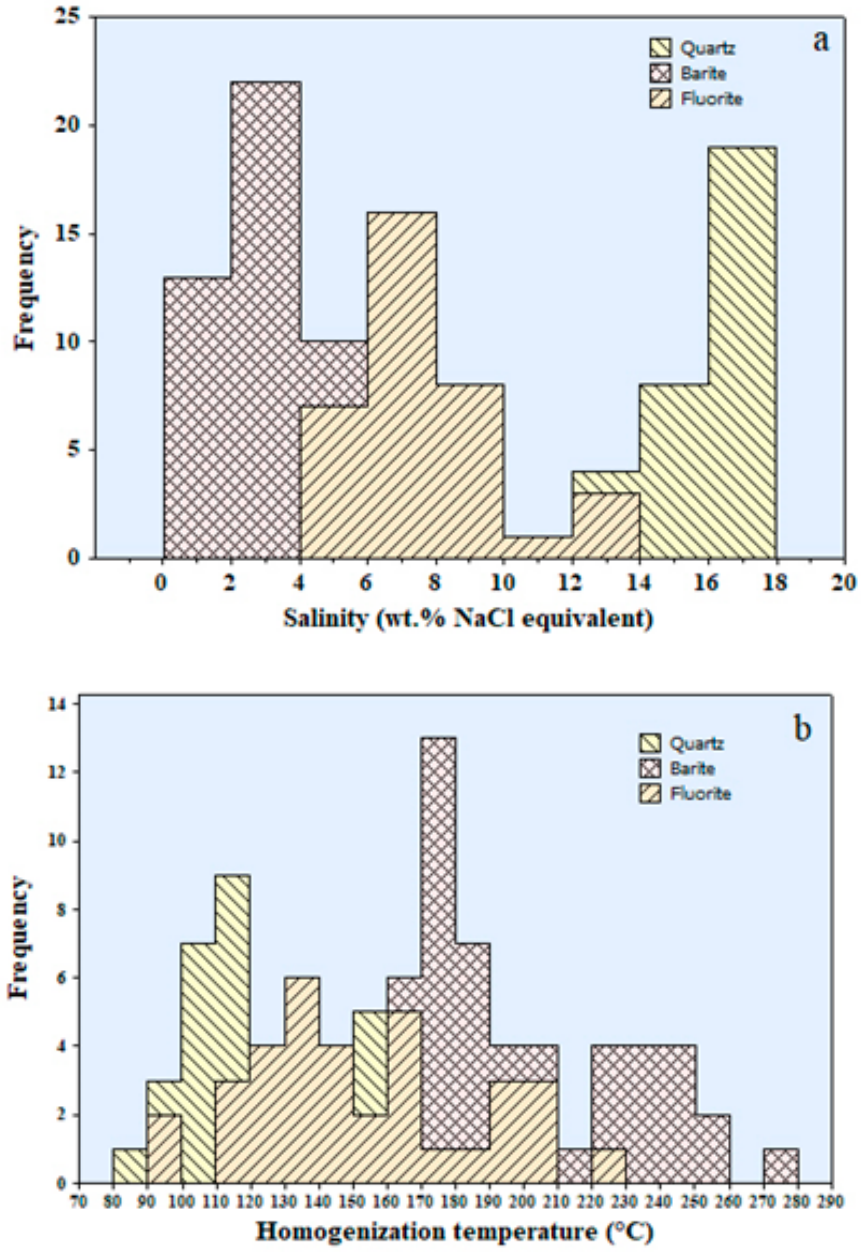

Figure 9. (**a**) Frequency histogram of salinity for fluid inclusions in barite, fluorite, and quartz samples. (**b**) Frequency histogram of homogenization temperatures for fluid inclusions in barite, fluorite, and quartz samples.

5. Discussion

5.1. REE Geochemistry

Since the concentration of most REEs in barite samples is below the detection limit, the chondrite-normalized REE patterns for barite samples are incomplete and unusable, which is why they are not produced. Nevertheless, two points can be inferred from the REE data in barite samples. First, the ∑REE concentration is low in these samples (14.80–19.59 ppm), and second, they are enriched in LREEs compared to HREEs. The enrichment of barite

with LREEs compared to HREEs is a common phenomenon and stems from the fact that the greater similarity of the LREE ionic radius to that of Ba^{2+} during REE substitution in the barite structure leads to LREE concentration in the barite [40].

The ΣREE concentration in barite can apparently be used as a criterion for determining the origin of barite. In general, terrestrial and hydrothermal barites have lower ΣREE concentrations compared to deep-marine barites [40]. The REE content in marine barites is generally 10 to 100 times higher than in barites formed on land [40,41]. Based on the ΣREE concentration, the Ardakan barite has a hydrothermal (terrestrial) and not a deep-marine origin, as it has a low ΣREE content (Table 1). Another geochemical index used to distinguish between marine and terrestrial barites is the Ce/La ratio. Deep-sea barites have similar Ce/La ratios to that of seawater (<1), while the terrestrial barites (vein barites) are characterized by higher Ce/La ratios, comparable to those of basic rocks and clays (>1 [40]). The Ce/La ratio in the barites from the Ardakan deposit ranges from 4.0 to 6.5 (Table 1), consistent with the terrestrial, rather than marine, origin of barites.

Like barite, the ΣREE concentration in fluorite is an indicator of the environment, so fluorites with low ΣREE content are interpreted as deriving from a sedimentary setting [42–45]. Although the REE concentration in fluorite samples is mostly below the detection limit, the maximum value of ΣREE based on the censored data is low (Table 2), indicating a sedimentary environment for fluorite. This conclusion is confirmed by the carbonate host rocks of the ore in the Ardakan deposit. Moreover, the Tb/Ca versus Tb/La diagram is used as a discrimination diagram to distinguish between fluorites with sedimentary, hydrothermal, and pegmatitic affinity [46,47]. All data points of fluorite samples are plotted in the hydrothermal field (Figure 10), indicating a hydrothermal origin. Although the Tb/Ca and Tb/La ratios for fluorite samples are calculated by replacing $\frac{3}{4}$ of the lower detection limit with censored Tb and La data, the censored data show that all true values for the Tb and La concentrations plot the fluorites in the hydrothermal field. The conclusions drawn from the REE geochemistry for barite and fluorite origin (hydrothermal) are, therefore, entirely consistent.

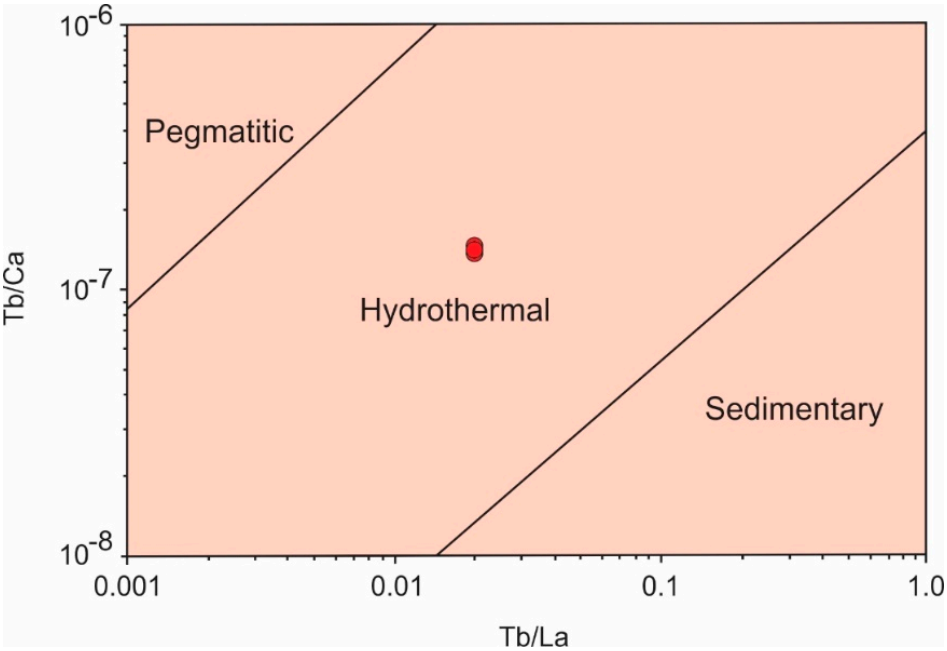

Figure 10. Tb/Ca versus Tb/La diagram for the fluorite samples from the Ardakan deposit (after [46,47]).

The geochemistry of REEs in the host rocks is similar to that of the barite samples in terms of the low ΣREE concentration, the enrichment with LREEs compared to HREEs (Figure 7), and the Ce/La ratio of more than unity (Table 3). These similarities could indicate

that Ba and/or the mineralizing fluids could originate from the host rocks. Nevertheless, the low Ba concentration in the host rocks (0.01–0.61% BaO; Table 3) rules out the possibility that all of the Ba in the Ardakan deposit originated from these rocks. The origin of Ba and mineralizing solutions will be discussed in the next sections. At the very least, the REE geochemical similarities between barites and the host rocks may indicate that mineralizing fluids have interacted with the host rocks prior to or during the barite deposition, as is also confirmed by the local silicification and baritization of the host rocks.

5.2. Source of Sulfur and Oxygen

Sulfur in geological materials ultimately comes from two main reservoirs, including magma (mantle) and seawater sulfate. The $\delta^{34}S$ value of the mantle is traditionally considered to be similar to the meteoritic composition of $0 \pm 2‰$. The igneous rocks show large variations in $\delta^{34}S$ values, but the majority of their $\delta^{34}S$ values cluster around 0‰ [48]. In contrast, the $\delta^{34}S$ values of seawater sulfate are strongly positive and vary greatly from a minimum value of +11‰ in the Permo-Triassic to a maximum value of +35‰ in the Precambrian–Cambrian [49]. The strong positive $\delta^{34}S$ values of the Ardakan barite samples (+27.9 to +32.4‰) indicate that the sulfur is not originated from a magmatic source but from seawater sulfate. Seawater sulfate is supplied directly from seawater for the precipitation of marine barite, whereas for epigenetic barite it is provided from basinal (connate) waters and/or Ca-sulfates in evaporites [8,25,50]. Comparison of the sulfur isotope data of barite samples with the $\delta^{34}S$ curve of seawater during geologic time shows that the data are consistent with the sulfur isotopic composition of Late Precambrian–Lower Cambrian seawater (Figure 11a). This indicates that the sulfur in the barite was most likely supplied from evaporites and/or connate waters in this age range. Surprisingly, the Late Precambrian (Dezu Formation) and Lower Cambrian rock units in the study area contain gypsum beds (Figure 2), which could supply the required sulfur for the formation of barite in the Ardakan deposit.

Similar to sulfur, the $\delta^{18}O$ values of the barite samples (+15.9 to +18.1‰) are significantly higher than the usual $\delta^{18}O$ values in igneous rocks (−1.2–+7.0; [51,52]), suggesting that the oxygen does not originate from the magma but must be supplied from seawater. The oxygen isotopic composition of seawater was not constant throughout Earth's history, as its $\delta^{18}O$ value changed from a minimum value of +10‰ in the Permian to a maximum value of +17‰ in the Late Devonian [49]. Although the sulfur isotopic data of the barite samples match well with the sulfur isotopic composition of the Late Precambrian–Lower Cambrian evaporites, their oxygen isotopic composition is slightly heavier than that of the evaporites (Figure 11b). This difference could be due to kinetic isotopic fractionation, bacterial sulfate reduction [53,54], or oxygen input from connate waters with heavier $\delta^{18}O$ values. The isotopic composition of oxygen shows, therefore, that oxygen in the barite was supplied either by Late Precambrian–Lower Cambrian evaporites or from basinal brines with somewhat heavier $\delta^{18}O$ values than these evaporites.

5.3. Source of the Mineralizing Fluids

Figure 12 shows the T_h–salinity diagram for fluid inclusions in barite, fluorite, and quartz from the Ardakan deposit. Although the temperature and salinity ranges of fluid inclusions overlap to some extent, the temperature–salinity field of each mineral is distinguishable, such that quartz precipitated from fluids with high salinity and low to mid temperature (12.85–16.89 wt.% NaCl equivalent and 90–165 °C), barite from fluids with low to mid salinity and mid to high temperature (0.88–9.21 wt.% NaCl equivalent and 138–270 °C), and fluorite from fluids with low to mid salinity and temperature (4.18–13.07 wt.% NaCl equivalent and 92–220 °C). The medium to high salinity of the fluid inclusions is consistent with the salinity of the basinal brines, while their low salinity indicates the dilution of the mineralizing fluids by meteoric water [55,56]. The temperature range of basinal brines varies depending on the depth from which they originate, from ambient to more than 300 °C [55,57,58]. The range of homogenization temperatures of fluid

inclusions hosted in barite, fluorite, and quartz (90–270 °C) is also compatible with the temperature of basinal brines. Sulfur and oxygen isotope data have already confirmed that these elements originated from evaporites and/or connate water.

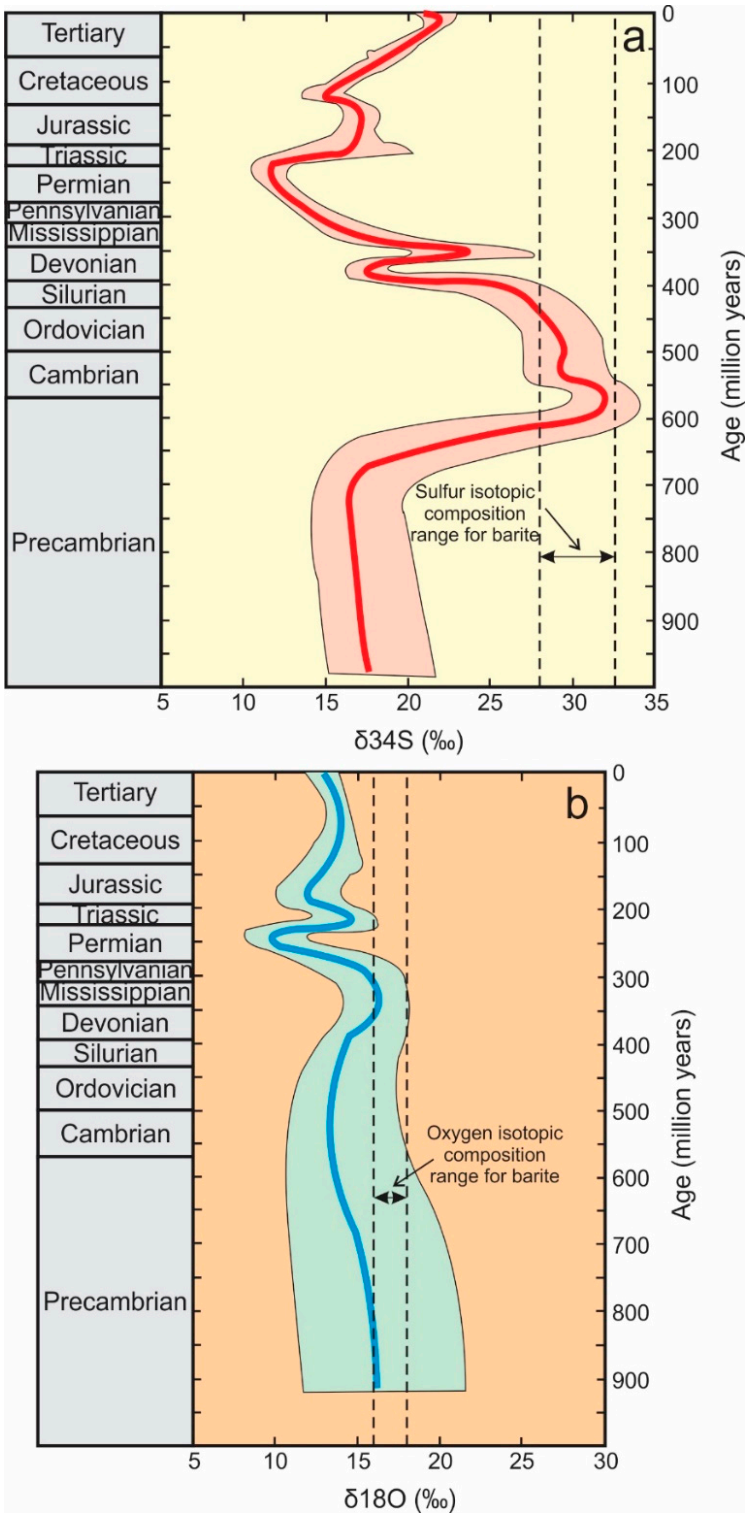

Figure 11. The $\delta^{34}S$ and $\delta^{18}O$ values of barite samples from the Ardakan deposit compared to the $\delta^{34}S$ (**a**) and $\delta^{18}O$ (**b**) curves of seawater [49]. The heavy lines are the best estimate of $\delta^{34}S$ and $\delta^{18}O$ of the seawater. The shaded areas are the uncertainty related to the curves.

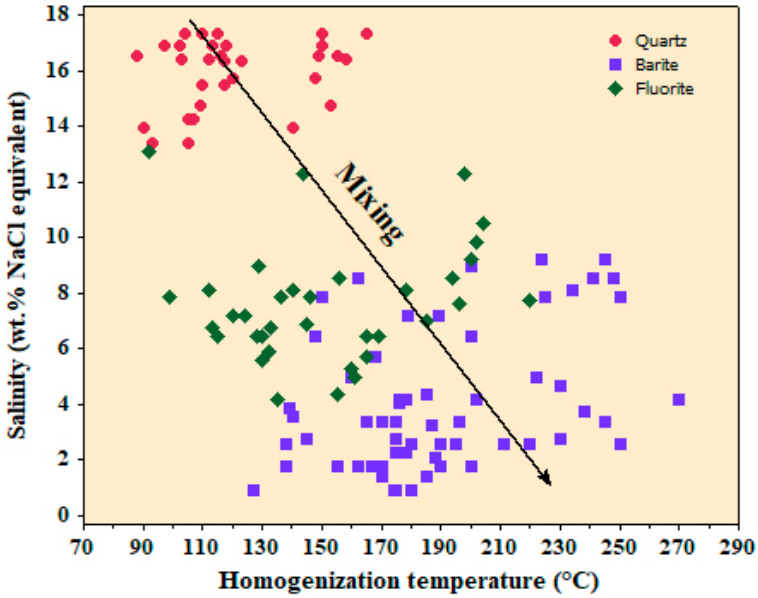

Figure 12. The T_h–salinity diagram for fluid inclusions in barite, fluorite, and quartz from the Ardakan deposit.

The trend of the data points in Figure 12 shows that a warmed, low-salinity meteoric water mixed with a cooler, more saline basinal brine. It is possible that the meteoric water first sank into the deep part of the basin, warmed up there, and then migrated upwards and mixed with the basinal fluids [25]. This leads to the conclusion that the mineralizing fluids in the Ardakan barite deposit were formed from basinal brines with the participation of meteoric water.

Although a paragenetic distinction between barite, fluorite, and quartz is not possible based on the textural and field evidence, the distribution of the homogenization temperature of fluid inclusions in these minerals indicates that the mineralization temperature of barite is the highest, followed by fluorite, while quartz mineralization occurred in the lowest temperature range. In relation to the salinity of the mineralizing fluids, this process is reversed, so that the precipitation of quartz occurred in the highest salinity of the fluid, followed by fluorite, and barite precipitated in the lowest salinity of the mineralizing fluids. It is possible that the precipitation of barite at the time when the temperature and salt content of the mineralizing fluid were at their highest and lowest values, respectively, reflects the low solubility of barite (about 2.5 mg/L at 25 °C; [59]), resulting in its faster precipitation compared to fluorite and quartz.

5.4. The Mode of Ore Formation

A comparison of the findings for the Ardakan deposit with those of the Ab Torsh barite deposit in Kerman province, Iran [25], shows that they have many similarities in terms of geological setting, epigenetic and stratabound nature, role of structural features in mineralization, host rock type, mineralogy, and source of sulfate and ore-forming fluids. The negligible differences are the younger age of the host rock for the Ab Torsh deposit (Senonian carbonates), and the presence of minor galena, pyrite, and bornite in the Ab Torsh deposit and more fluorite and minor sphalerite in the Ardakan deposit. These basic similarities suggest that the mode of formation for these deposits should also be the same. In the case of Ab Torsh, Kalantar Hormozi et al. [25] concluded that severe faulting and brecciation of the host rocks by compressional tectonics formed the channel ways for the upward migration of deep basinal brines that acted as mineralizing fluids. Barite precipitated where these ascending hot, Ba-bearing hydrothermal fluids met the cooler, sulfate-bearing connate waters above and/or the descending cold sulfate-bearing meteoric waters ([25]; their Figure 9).

The field investigations, including the brecciated host rock cemented by barite (Figure 5d), demonstrate an epigenetic origin and syn- to post-faulting mineralization for the Ardakan deposit. As already mentioned, the Ardakan deposit area is a highly faulted and tectonized area, so that even the Precambrian rock units are thrusted over the younger ones by the deep faults (Figure 2). The fact that mineralization occurred parallel to the main faults and thrusts may indicate the role of these structures in mineralization. It is likely that mineralization occurred in some preexisting faults. Given that the age of the host rock is Middle Triassic, post-Triassic compressive tectonic movements should be considered more effective for mineralization. Since the sulfur isotope data show that the sulfate in the Ardakan deposit is probably derived from Late Precambrian–Lower Cambrian evaporites, and the fluid inclusion data indicate that heated meteoric water and cooler connate water were involved in the mineralization process, it is likely that the meteoric water penetrated deep into the basin and, as it heated, dissolved the sulfates in the Late Precambrian–Lower Cambrian strata and transported them upward. The meeting of these sulfate-containing meteoric waters with colder, Ba-, F-, and silica-containing connate waters [60–62] in the overlying Middle Triassic dolomites caused the precipitation of barite and associated minerals. In addition to deposits in which barite is the main mineral, this model of ore genesis is also considered for shallow ore veins or unconformity-related Pb–Zn deposits with fluorite and barite [2,45,63,64].

The Middle Triassic Shotori Formation, in which the barite mineralization occurs, and the overlying Middle Triassic Espahak Limestone are unconformably overlain by a rock unit from the Upper Triassic to the late Lower Jurassic. In fact, the barite mineralization took place below an unconformity surface. Therefore, the Ardakan deposit can be classified in the structure-related class of the classification scheme for barite deposits by Dill [2]. As fluorite and minor sphalerite are associated with barite, the Ardakan deposit shows a tendency towards the unconformity-related (shallow veins) Pb–Zn–Ba–fluorite subclass.

6. Conclusions

The Ardakan deposit occurs as a stratabound and epigenetic barite deposit in dolomites and limestones of the Middle Triassic Shotori Formation. The geochemistry of the REEs, including the low ΣREE content and Ce/La ratio, suggest a hydrothermal (terrestrial) origin of the barite. The geochemical REE indicators (Tb/Ca and Tb/La ratios and low ΣREE concentration) also confirm a hydrothermal source in a sedimentary environment for the associated fluorite. The S and O isotope data indicate that sulfur and oxygen in the barite originated from evaporites and/or connate waters of Late Precambrian–Lower Cambrian age, or, in the case of oxygen, from basinal brines with slightly heavier $\delta^{18}O$ values than these evaporites. The microthermometric results of the fluid inclusion studies reveal that the mineralizing fluids in the Ardakan deposit are sourced from basinal brines with a contribution of heated meteoric water. Based on the available data, it is concluded that the Ardakan barite deposit was created where the warmed, upwelling sulfate-bearing meteoric water met cooler, Ba-bearing connate water trapped in the overlying Middle Triassic dolomites and limestones. The post-Triassic tectonic movements provided the force for the derivation of the mineralizing solutions and the channels necessary for their movement through intense faulting and brecciation of the host rocks. The Ardakan deposit is classified in the structure-related class and the unconformity-related subclass of barite deposits.

Author Contributions: Conceptualization, F.E., G.R.P. and S.M.K.; investigation, E.A. and F.E.; resources, E.A.; data curation, F.E., G.R.P. and S.M.K.; writing—original draft preparation, E.A.; writing—review and editing, F.E., G.R.P. and S.M.K.; supervision, F.E. All authors have read and agreed to the published version of the manuscript.

Funding: This research received no external funding.

Data Availability Statement: The original data are included in the article; further inquiries can be directed to the corresponding authors.

Acknowledgments: This research was conducted as a partial fulfilment of the requirements for a Ph.D. in economic geology for the first author from Behbahan Branch, Islamic Azad University. We thank the manager and staff of Barit-e Falat-e Iran Company for the opportunity of field research and accommodation.

Conflicts of Interest: The authors declare no conflicts of interest.

References

1. Brobst, D.A. Barium minerals. In *Industrial Minerals and Rocks*, 6th ed.; Carr, D.D., Ed.; Society for Mining, Metallurgy & Exploration: Littleton, CO, USA, 1994; pp. 125–134.
2. Dill, H.G. The 'chessboard' classification scheme of mineral deposits: Mineralogy and geology from aluminum to zirconium. *Earth-Sci. Rev.* **2010**, *100*, 1–420.
3. Johnson, C.A.; Piatak, N.M.; Miller, M.M. Barite (Barium). In *Critical Mineral Resources of the United States—Economic and Environmental Geology and Prospects for Future Supply*; Schulz, K.J., DeYoung, J.H., Jr., Seal, R.R., II, Bradley, D.C., Eds.; U.S. Geological Survey Professional Paper 1802; U.S. Geological Survey: Reston, VA, USA, 2017; Chapter D; pp. D1–D18.
4. Ebunu, A.I.; Olanrewaju, Y.A.; Ogolo, O.; Adetunji, A.R.; Onwualu, A.P. Barite as an industrial mineral in Nigeria: Occurrence, utilization, challenges, and prospects. *Heliyon* **2021**, *7*, e07365. [CrossRef]
5. McRae, M.E. *Barite. 2018 Minerals Yearbook*; BARITE [ADVANCE RELEASE]; U.S. Geological Survey: Reston, VA, USA, 2021.
6. McRae, M.E. *Barite. Mineral Commodity Summaries*; U.S. Geological Survey: Reston, VA, USA, 2022.
7. Faure, G. *Principles and Applications of Geochemistry*; Prentice Hall: Upper Saddle River, NJ, USA, 1998; 600p.
8. Hanor, J.S. Barite-celestine geochemistry and environments of formation. *Rev. Mineral. Geochem.* **2000**, *40*, 193–275. [CrossRef]
9. Paytan, A.; Mearon, S.; Cobb, K.; Kastner, M. Origin of marine barite deposits: Sr and S isotope characterization. *Geology* **2002**, *30*, 747–750. [CrossRef]
10. Griffith, E.M.; Paytan, A.; Wortmann, U.G.; Eisenhauer, A.; Scher, H.D. Combining metal and nonmetal isotopic measurements in barite to identify mode of formation. *Chem. Geol.* **2018**, *500*, 148–158. [CrossRef]
11. Brobst, D.A. *Barite Resources of the United States*; U.S. Geological Survey Bulletin 1072-B; U.S. Government Printing Office: Washington, DC, USA, 1958; 130p.
12. Clark, S.H.B.; Gallagher, M.J.; Poole, F.G. World barite resources—A review of recent production patterns and a genetic classification. *Trans. Inst. Min. Metall.-Sect. B-Appl. Earth Sci.* **1990**, *99*, B125–B132.
13. Ghorbani, M. *The Economic Geology of Iran, Mineral Deposits and Natural Resources*; Springer: Dordrecht, The Netherlands, 2013; 542p.
14. Rajabzadeh, M.A. A fluid inclusion study of a large MVT barite–fluorite deposit: Komshecheh, Central Iran. *Iran. J. Sci. Technol. Trans.* **2007**, *31*, 73–87.
15. Ehya, F. Rare earth element and stable isotope (O, S) geochemistry of barite from the Bijgan deposit, Markazi Province, Iran. *Min. Petrol.* **2012**, *104*, 81–93. [CrossRef]
16. Zarasvandi, A.; Zaheri, N.; Pourkaseb, H.; Chrachi, A.; Bagheri, H. Geochemistry and fluid-inclusion microthermometry of the Farsesh barite deposit. *Iran. Geol.* **2014**, *20*, 201–214.
17. Ehya, F.; Mazraei, S.M. Hydrothermal barite mineralization at Chenarvardeh deposit, Markazi Province, Iran: Evidences from REE geochemistry and fluid inclusions. *J. Afr. Earth Sci.* **2017**, *134*, 299–307. [CrossRef]
18. Alaminia, Z.; Sharifi, M. Geological, geochemical and fluid inclusion studies on the evolution of barite mineralization in the Badroud area of Iran. *Ore Geol. Rev.* **2018**, *92*, 613–626. [CrossRef]
19. Behyari, M.; Rahimsouri, Y.; Hoseinzadeh, E.; Kurd, N. Evaluating of lithological and structural controls on the barite mineralization by using the remote sensing, Fry and fractal methods, Northwest Iran. *Arab. J. Geosci.* **2019**, *12*, 1–11. [CrossRef]
20. Derakhshi, M.G.; Hosseinzadeh, M.R.; Moayyed, M.; Maghfouri, S. Geological, isotope geochemical and fluid inclusion constraints on the Mishu SEDEX-type Barite (Pb-Cu-Zn) system, NW Iran. *Ore Geol. Rev.* **2020**, *121*, 103493. [CrossRef]
21. Hodaie Keveshk, H.; Ehya, F.; Rostami Paydar, G.; Maleki Kheymehsari, S. Rare earth elements geochemistry, O and S isotopic compositions, and microthermometric data of barite from the Kuh-Ghalagheh deposit, Markazi Province, Iran. *Appl. Geochem.* **2021**, *135*, 105128. [CrossRef]
22. Hodaie Keveshk, H.; Ehya, F.; Rostami Paydar, G.; Maleki Kheymehsari, S. The Kohlou barite deposit, Markazi Province, Iran: Studies on rare earth element geochemistry, O and S isotopes, and fluid inclusions. *Carbonates Evaporites* **2022**, *37*, 38. [CrossRef]
23. Sharifiyan, S.; Hosseinzadeh, M.R.; Maghfouri, S.; Moayyed, M. Sediment hosted stratiform barite—(Cu-Zn-Pb) deposits in the southwest Mahabad, Iran; implications for geology, ore textural, compositional, and S-O isotopes geochemistry. *Ore Geol. Rev.* **2021**, *139 Pt B*, 104549. [CrossRef]
24. Alizadeh, A.; Hoseini, C.; Haji, E. Structural Conditions for Localization of Barite Mineralization in Tectonic Evolution of the Southern Sanandaj Zone, Iran. *Geotectonics* **2023**, *57*, 820–834. [CrossRef]
25. Kalantar Hormozi, H.; Ehya, F.; Rostami Paydar, G.; Maleki Kheymehsari, S. Formation of barite in the Ab Torsh deposit, Kerman province, Iran: Insights from rare earth elements, O and S isotopes, and fluid inclusions. *Geochemistry* **2023**, *83*, 126024. [CrossRef]
26. Liu, Y.; Song, Y.; Fard, M.; Hou, Z.; Ma, W.; Yue, L. The Characteristics and Origin of Barite in the Giant Mehdiabad Zn-Pb-Ba Deposit, Iran. *Econ. Geol.* **2023**, *118*, 1495–1519. [CrossRef]

27. Rahimpour Bonab, H.; Shekarifard, A. Barite Ore Deposits in the Central Iran-Ardakan Province: Genesis and Alterations. *Iran. Int. J. Sci.* **2002**, *3*, 69–91.
28. Shekarifard, A.; Rahimpour Bonab, H.; Rohshahbaz, J. Alteration of sulfide minerals in the Ardakan barite-chalcopyrite ore deposits. *Iran. J. Crystal. Mineral.* **2004**, *12*, 143–158. (In Persian with English Abstract)
29. Yousefi, M.; Jafarian, M.B. *(Compilers) Geological Map of Iran 1:100000 Series Sheet No. 6854 (Ardakan)*; Geological Survey of Iran: Tehran, Iran, 2005.
30. Ghorbani, M. Geological Setting and Crustal Structure of Iran. In *The Geology of Iran: Tectonic, Magmatism and Metamorphism. Earth and Environmental Sciences Library*; Springer: Cham, Switzerland, 2021.
31. Berberian, M. Chapter 9—Active Tectonics and Geologic Setting of the Iranian Plateau. In *Developments in Earth Surface Processes*; Berberian, M., Ed.; Elsevier: Amsterdam, The Netherlands, 2014; Volume 17, pp. 151–171.
32. Alavi, M. *Tectonic Map of the Middle East 1:5,000,000*; Geological Survey of Iran: Tehran, Iran, 1991.
33. Aghanabati, S.A. *Geology of Iran*; Geological Survey of Iran: Tehran, Iran, 2004; 586p. (In Persian)
34. Lawler, J.P.; Crawford, M.L. Stretching of fluid inclusions resulting from a low-temperature microthermometric technique. *Econ. Geol.* **1983**, *78*, 527–529. [CrossRef]
35. Bodnar, R.J. Revised equation and table for determining the freezing point depression of H_2O-NaCl solution. *Geochim. Cosmochim. Acta* **1993**, *57*, 683–684. [CrossRef]
36. Boynton, W.V. Geochemistry of the rare earth elements: Meteorite studies. In *REE Geochemistry*; Henderson, P., Ed.; Elsevier: Amsterdam, The Netherlands, 1984; pp. 63–114.
37. Roedder, E. Fluid inclusions. *Rev. Miner.* **1984**, *12*, 644.
38. Shepherd, T.J.; Ranbin, A.H.; Alderton, D.H.M. *A Practical Guide to Fluid Inclusion Studies*; Blackie: Glasgow, UK, 1985; 239p.
39. Goldstein, R.H.; Reynolds, T.J. *Systematics of Fluid Inclusions in Diagenetic Minerals*; Society of Sedimentary Geology Short Course; Sepm Society for Sedimentary: Claremore, OK, USA, 1994; Volume 31, 199p.
40. Guichard, F.; Church, T.M.; Treuil, M.; Jaffrezic, H. Rare earths in barites: Distribution and effects on aqueous partitioning. *Geochim. Cosmochim. Acta* **1979**, *43*, 983–997. [CrossRef]
41. Dora, M.L.; Roy, S.K.; Khan, M.; Randive, K.; Kanungo, D.R.; Barik, R.; Kaushik, C.S.; Bari, S.H.; Pattanayak, R.S.; Krishna, K.V.S.; et al. Rift-induced structurally controlled hydrothermal barite veins in 1.6 Ga granite, Western Bastar Craton, Central India: Constraints from fluid inclusions, REE geochemistry, sulfur and strontium isotopes studies. *Ore Geol. Rev.* **2022**, *148*, 105050. [CrossRef]
42. Hill, G.T.; Andrew, R.C.; Philip, R.K. Geochemistry of southwestern New Mexico fluorite occurrences: Implications for precious metals exploration in fluorite-bearing systems. *J. Geochem. Explor.* **2000**, *68*, 1–20. [CrossRef]
43. Ronchi, L.H.; Tauray, J.C.; Michard, A.; Dardenne, M.A. The Ribeira fluorite district, Southern Brazil: Geological and geochemical (REE, Sm–Nd isotopes) characteristics. *Miner. Depos.* **1993**, *28*, 240–252. [CrossRef]
44. Sasmaz, A.; Önal, A.; Sagiroglu, A.; Önal, M.; Akgul, B. Origin and nature of the mineralizing fluids of thrust zone fluorites in Celikhan (Adiyaman, Eastern Turkey): A geochemical approach. *Geochem. J.* **2005**, *39*, 131–139. [CrossRef]
45. Ehya, F. Variation of mineralizing fluids and fractionation of REE during the emplacement of the vein-type fluorite deposit at Bozijan, Markazi Province, Iran. *J. Geochem. Explor.* **2012**, *112*, 93–106. [CrossRef]
46. Möller, P.; Parekh, P.P.; Schneider, H.J. The application of Tb/Ca–Tb/La abundance ratios to problems of fluorspar genesis. *Miner. Depos.* **1976**, *11*, 111–116. [CrossRef]
47. Möller, P.; Morteani, G. On the chemical fractionation of REE during the formation of Ca-minerals and its application to problems of the genesis of ore deposits. In *The Significance of Trace Elements in Solving Petrogenetic Problems*; Augustithis, S., Ed.; Theophrastus Publications: Athens, Greece, 1983; pp. 747–791.
48. Seal, R.R. Sulfur isotope geochemistry of sulfide minerals. *Rev. Mineral. Geochem.* **2006**, *61*, 633–677. [CrossRef]
49. Claypool, G.E.; Holser, W.T.; Kaplan, I.R.; Sakai, H.; Zak, I. The age curves of sulfur and oxygen isotopes in marine sulfate and their mutual interpretation. *Chem. Geol.* **1980**, *28*, 199–260. [CrossRef]
50. Warren, J.K. Evaporites, brines and base metals: Fluids, flow and 'the evaporite that was'. *Aust. J. Earth Sci.* **1997**, *44*, 149–183. [CrossRef]
51. Taylor, H.P. The oxygen isotope geochemistry of igneous rocks. *Contrib. Mineral. Petrol.* **1968**, *19*, 1–71. [CrossRef]
52. Boroughs, S.; Wolff, J.A.; Ellis, B.S.; Bonnichsen, B.; Larson, P.B. Evaluation of models for the origin of Miocene low-$\delta^{18}O$ rhyolites of the Yellowstone/Columbia River Large Igneous Province. *Earth Planet. Sci. Lett.* **2012**, *313–314*, 45–55. [CrossRef]
53. Mandernack, K.W.; Krouse, H.R.; Skei, J.M. A stable sulfur and oxygen isotopic investigation of sulfur cycling in an anoxic marine basin, Framvaren Fjord, Norway. *Chem. Geol.* **2003**, *195*, 181–200. [CrossRef]
54. Johnson, C.A.; Emsbo, P.; Poole, F.G.; Rye, R.O. Sulfur-and oxygen-isotopes in sediment-hosted stratiform barite deposits. *Geochem. Cosmochim. Acta* **2009**, *73*, 133–147. [CrossRef]
55. Bodnar, R.J. Hydrothermal solutions. In *Encyclopedia of Geochemistry*; Marshall, C.P., Fairbridge, R.W., Eds.; Kluwer Academic Publishers: Lancaster, PA, USA, 1999; pp. 333–337.
56. González-Sánchez, F.; González-Partida, E.; Canet, C.; Atudorei, V.; Alfonso, P.; Morales-Puente, P.; Cienfuegos-Alvarado, E.; González-Ruiz, L. Geological setting and genesis of stratabound barite deposits at Múzquiz, Coahuila in northeastern Mexico. *Ore Geol. Rev.* **2017**, *81*, 1184–1192. [CrossRef]

57. Gleeson, S.A.; Yardley, B.W.D.; Munz, I.A.; Boyce, A.J. Infiltration of basinal fluids into high-grade basement, South Norway: Sources and behaviour of waters and brines. *Geofluids* **2003**, *3*, 33–48. [CrossRef]
58. Kyser, T.K. Fluids, basin analysis, and mineral deposits. *Geofluids* **2007**, *7*, 238–257. [CrossRef]
59. Dunn, K.; Daniel, E.; Shuler, P.J.; Chen, H.J.; Tang, Y.; Yen, T.F. Mechanisms of surface precipitation and dissolution of barite: A morphology approach. *J. Colloid Interface Sci.* **1999**, *214*, 427–437. [CrossRef] [PubMed]
60. Oliver, J. Fluids expelled tectonically from orogenic belts, their role in hydrocarbon migration and other geological phenomena. *Geol.* **1986**, *14*, 99–102. [CrossRef]
61. Leach, D.L.; Bradley, D.C.; Huston, D.; Pisarevsky, S.A.; Taylor, R.D.; Gardoll, S.J. Sediment-hosted lead–zinc deposits in Earth history. *Econ. Geol.* **2010**, *105*, 593–625. [CrossRef]
62. Leach, D.L.; Sangster, D.F.; Kelley, K.D.; Large, R.R.; Garven, G.; Allen, C.R.; Gutzmer, J.; Walters, S. Sediment-hosted lead–zinc deposits: A global perspective. In *Economic Geology 100th Anniversary Volume*; Society of Economic Geologists, Inc.: Littleton, CO, USA, 2005; pp. 561–607.
63. Galindo, C.; Tornos, F.; Darbyshire, D.P.F.; Casquet, C. The age and origin of the barite-fluorite (Pb-Zn) veins of the Sierra del Guadarrama (Spanish Central System, Spain): A radiogenic (Nd, Sr) and stable isotope study. *Chem. Geol.* **1994**, *112*, 351–364. [CrossRef]
64. Nejadhadad, M.; Taghipour, B.; Lentz, D.R. Implications of multiple fluids in the deposition of Pb-Zn-Ba deposits in the Alvand Mountain, Golpayegan, Iran: Evidence from fluid inclusions and O, C, S isotopes. *Ore Geol. Rev.* **2023**, *153*, 105300. [CrossRef]

Disclaimer/Publisher's Note: The statements, opinions and data contained in all publications are solely those of the individual author(s) and contributor(s) and not of MDPI and/or the editor(s). MDPI and/or the editor(s) disclaim responsibility for any injury to people or property resulting from any ideas, methods, instructions or products referred to in the content.